Technical Design Report for E70

Tomofumi NAGAE [a] (Spokesperson), S. Kanatsuki,[a] H. Ekawa,[a] T. Nanamura,[a]
A. Koshikawa, [a] H. Fujioka, [a] M. Naruki,[a] S. Hasegawa,[b] K. Hosomi,[b] Y. Ichikawa,[b]
K. Imai,[b] H. Sako,[b] S. Sato,[b] K. Tanida,[b] J. Yoshida, [b] S.H. Hayakawa,[c] M. Nakagawa,[c]
Y. Nakada,[c] T. Akaishi,[c] A. Sakaguchi,[c] Y. Akazawa,[d] M. Fujita,[d] R. Honda,[d] K. Miwa,[d]
H. Kanauchi,[d] H. Tamura,[d] T. Gogami,[d] S.N. Nakamura, [d] M. Kaneta, [d] S. Nagao, [d]
Y. Toyama, [d] K. Itabashi, [d] K. Aoki,[e] E. Hirose, [e] H. Takahashi, [e] T. Takahashi,[e] M. Ukai,[e]
T.O. Yamamoto,[e] J.K. Ahn,[f] S.H. Kim [f] H.M. Yang,[f] K.Y. Roh,[f] M. Agnello, [q]
E. Botta,[gm] A. Feliciello,[g] P. Evtoukhovitch,[h] Z. Tsamalaidze,[h] J.Y. Lee,[i] T. Moon,[i]
S. Kimbara,[j] T. Hasegawa,[k] K. Shirotori,[l] M. Yosoi, [l] D. Shoukavy, [n] L. Tang[op]
– J-PARC E70 Collaboration –

[a] *Department of Physics, Kyoto University, Kitashirakawa, Kyoto 606-8502, Japan*
[b] *ASRC, JAEA, Tokai, Ibaraki 319-1195, Japan*
[c] *Department of Physics, Osaka University, Toyonaka, Osaka 560-0043, Japan*
[d] *Department of Physics, Tohoku University, Sendai 980-8578, Japan*
[e] *IPNS, KEK, Tsukuba, Ibaraki 305-0801, Japan*
[f] *Korea University, Seoul 136-713, Korea*
[g] *INFN Sezione di Torino, 10125 Torino, Italy*
[h] *JINR, Dubna, Russia*
[i] *Department of Physics and Astronomy, Seoul National University, Seoul 151-747, Korea*
[j] *Faculty of Education, Gifu University, Gifu 501-1193, Japan*
[k] *Kitasato University, Sagamihara, Japan*
[l] *RCNP, Osaka University, Ibaraki, Osaka 567-0047 Japan*
[m] *Università di Torino, 10124 Torino, Italy*
[n] *B.I. Stepanov Institute of Physics, National Academy of Sciences of Belarus, Belarus*
[o] *Department of Physics, Hampton University, Hampton, Virginia 23668, U.S.A.*
[p] *Thomas Jefferson National Accelerator Facility (JLab), Newport News, Virginia 23606, U.S.A.*
[q] *Politecnico di Torino, Torino 10129, Italy*

(Received January 16, 2019)

This report describes the technical details of the E70 experiment and beam time requests.

1. Physics Motivations of E70

1.1 Ξ-N Interaction

One of the important goals of hypernuclear spectroscopy is to establish a modern picture of generalized nuclear force models in relation to quantum chromo-dynamics (QCD) by extending the nucleon-nucleon force in flavor $SU(3)$. The forces between two octet baryons, such as N-N, Y-N, Y-Y, are its subjects. Here the Y stands for a baryon with strangeness, that is a hyperon (Λ, Σ, Ξ). Because of the short life time (10^{-10} sec.) of the hyperons, it is difficult to carry out Y-N, Y-Y scattering measurements. Therefore, we have been investigating the spectroscopy of hypernuclei to extract the information on the Y-N and Y-Y interactions. For example, the fine structure of p-shell Λ hypernuclei has revealed spin-dependent interactions of Λ-N force [1]. A precious information on the Λ-Λ force was obtained in the "Nagara" event in emulsion [2, 3]. Knowing that the Σ-N force is repulsive on average [4], the last key information is the Ξ-N interaction, which is the major subject in E70

experiment.

In a recent study of Lattice QCD calculations [5], the Ξ-N interaction potentials are available for various $S = -2$ channels, although the pion mass involved in the calculations is still large compared to its physical mass. Such a comparison between theory and experiment in near future would be very much interesting.

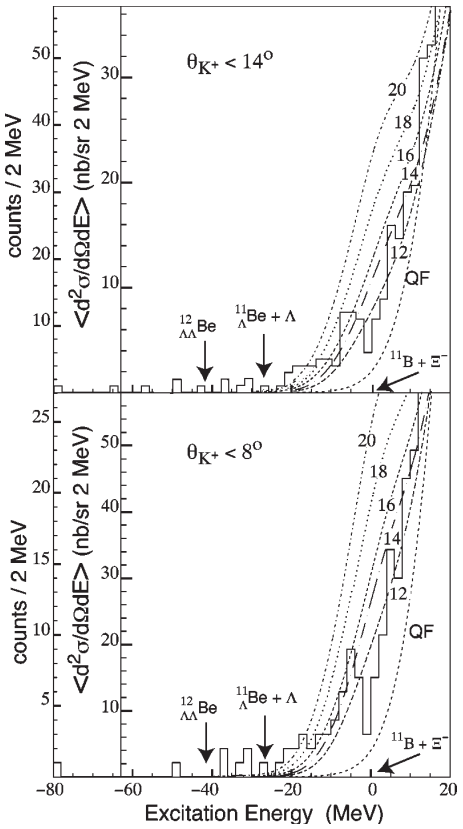

Fig. 1. Excitation-energy spectra from E885 for ^{12}C(K^-, K^+) X reaction for $\theta_{K^+} < 14°$ (top) and $\theta_{K^+} < 8°$(bottom) [10]. Theoretical curves for the different Ξ potential depths equal to 20, 18, 16, 14 and 12 MeV were superimposed.

1.2 Hyperon Puzzle

In the nuclear matter at the density of 2–3 times the nuclear saturation density, ρ_0, the strangeness degrees of freedom should play an essential role. Such a high-density condition is believed to be realized in the core of neutron stars. At such high density, the neutron Fermi energy would become larger than the mass difference between a Λ hyperon (1115 MeV/c^2) and a nucleon (939 MeV/c^2) and a lot of strangeness, Λ hyperons, would be created because of the attractive potential, U_Λ felt by the Λ hyperons in high density neutron matter. Thereby, the Fermi pressure would be reduced by strangeness degrees of freedom. The experimental information on U_Λ was obtained to be 30±1 MeV from the binding energy of heavy Λ hypernuclei up to $^{208}_{\Lambda}$Pb [6].

Another important feature of the strangeness is that s quark has negative charge of $-1/3e$. Therefore the hyperons have negative charge states such as Σ^- and Ξ^-. In the case of nucleons, proton and neutron, with *up* $(+2/3e)$ and *down* $(-1/3e)$ quarks, there are no negatively charged baryons. Thus, from the charge neutrality condition, the number of electrons can be converted to the number

of negative hyperons which greatly reduce the electron Fermi energy in the chemical balance of

$$\frac{{p_F^e}^2}{2m_e} + m_e = \frac{{p_F^Y}^2}{2m_Y} + m_Y + U_Y. \quad (1)$$

Here, it is important to know the hyperon potential depths, U_Y. The lightest negative hyperon, Σ^- (1197.4 MeV/c^2), has strongly repulsive potential of $U_\Sigma \sim +30$ MeV. Therefore, the Σ^- would not appear in neutron stars. The next candidate is Ξ^- (1321.7 MeV/c^2). At this moment, we have no definite information on the U_Ξ. Therefore, it is awaited to have a good estimate of U_Ξ from the binding energy measurements of the Ξ hypernuclei.

Based on the present knowledge of hypernuclei mentioned above, it is believed that the appearance of strangeness in such high-density nuclear matter is unavoidable and leads to the "Soft" equation of state (EoS). From the softening of the nuclear matter at high density, the maximum mass of neutron stars cannot exceeds 1.4×$M_\odot$. Therefore, recent observations of 2×$M_\odot$ neutron stars [7, 8] have a serious problem, called "Hyperon Puzzle".

1.3 Experimental Information on Ξ−hypernuclei

The experimental information on Ξ−hypernuclei has been very much limited so far. The missing-mass measurements with the ^{12}C(K^-, K^+) reaction were carried out at KEK [9] and BNL [10], although the statistics and the energy resolution were poor; energy resolution of the former case was σ =9.5 MeV and of the latter case was 6.1 MeV. Nevertheless, the E885 experiment observed about 42–67 events in the bound region $20 > B_\Xi > 0$ MeV and claimed evidence of the bound state(Fig. 1). Provided the Woods-Saxon type of the potential form, an initial analysis by BNL E885 group suggested an attractive Ξ potential with a depth of about 14 MeV. It might lead to a bound state at the binding energy of about 4.5 MeV. A reanalysis by Kohno *et al.* suggested almost zero [11] or even a weakly repulsive potential [12].

Recently, KEK E373 group discovered the "Kiso" event [13], as the first evidence of a deeply-bound Ξ^-−^{14}N system in the reaction Ξ^-−^{14}N→$^{10}_{\Lambda}$Be and $^{5}_{\Lambda}$He. The binding energy was estimated to be 3.87 ± 0.21 MeV, by assuming both $^{10}_{\Lambda}$Be+$^{5}_{\Lambda}$He are in the ground state. which was definitely larger than the Ξ^-−^{14}N atomic binding energy of 0.17 MeV(2p atomic orbit). Please note that the binding energies of the ground state and excited state of $^{10}_{\Lambda}$Be have been updated with the most recent values reported by the JLab E05-115 [14]. Even in the case that the $^{10}_{\Lambda}$Be is in the excited state, the binding energy is 1.03±0.18 MeV. Therefore it seems that a strongly-bound Ξ^-−^{14}N state exists, although the binding energy has an ambiguity. There is also an ambiguity from the strong conversion width induced by the $\Xi^- + p \to \Lambda\Lambda$ process. Therefore, it is difficult to determine the binding energy from a single event.

1.4 Coupling between Ξ− hypernuclei and double−Λ hypernuclei

There could exist couplings between two systems of S =−2, Ξp and $\Lambda\Lambda$, through a strong conversion process of $\Xi N \to \Lambda\Lambda$ [15]. Their masses are separated only by 28.62 MeV in vacuum (Fig. 2). Depending on the coupling strength, a part of the production strength of Ξ−hypernucleus state is used to excite the excited levels of double-Λ hypernucleus. Further, the energy levels of two-states would be attracted to make their separation narrower (of the order of 100 keV). Therefore, the coupling strength is determined with the production cross section ratio between the two states and the energy separation of two states.

2. History of E05 –Spectrometers

We, originally, planned to construct the SKS+ spectrometer system by adding a small dipole magnet in front of the SKS spectrometer as shown in Fig. 3. However the primary beam intensity

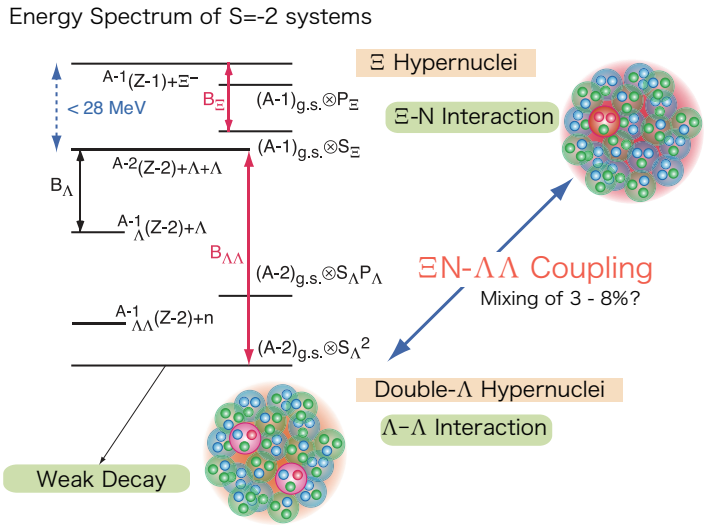

Fig. 2. Schematic energy spectrum of $S = -2$ hypernuclei. The Ξ hypernuclei and double-Λ hypernuclei are only separated by 28.62 MeV, and couple through the $\Xi^- p \to \Lambda\Lambda$ interaction.

from the J-PARC main ring (MR) was significantly lower than expected in the early stage of the MR beam commissioning. Therefore, we tried to increase the acceptance of the spectrometer to compensate the low primary beam intensity; at the same time we tried to improve the momentum resolution. Fortunately, in 2011 we succeeded to obtain a grant budget of about 3 million dollars to construct a new spectrometer dedicated to the study of the (K^-, K^+) reaction. We call it "Strangeness -2 Spectrometer (S-2S)". As shown in Table I, the performance of the S-2S supersedes that of SKS+ in all aspects. Based on this change, we presented a revised run plan upon the PAC request considering the realistic beam conditions, during the 13th PAC meeting in January, 2012.

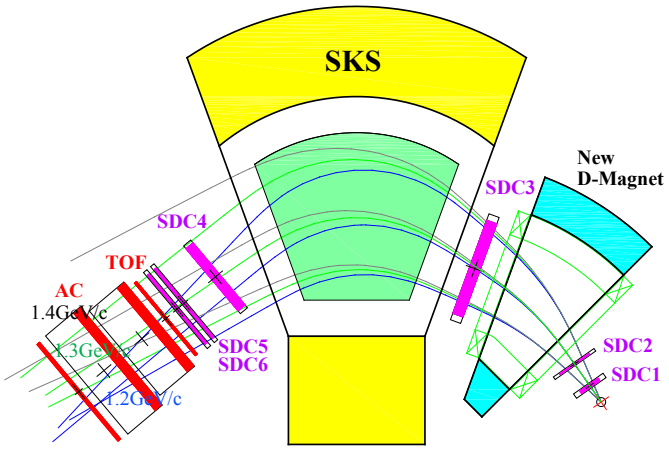

Fig. 3. Schematic view of the E05 setup, SKS+, in the original proposal.

In this situation, we requested an E05 pilot run for the ^{12}C(K^-, K^+) reaction at 1.8 GeV/c by using the existing SKS spectrometer, at the 19th PAC meeting in December, 2014. While the beam

Performance	SKS+	S-2S	SKS
Acceptance (msr)	30	55	110
Missing-mass resolution (FWHM)	3 MeV	$\lesssim$2 MeV	6 MeV
Magnet Configuration	DD	QQD	D

Table I. Comparison of two spectrometers: SKS+ in the original proposal and S-2S . In the last column, the SKS performance in the E05 run is listed for comparison.

power of the primary beam from MR was only 39 kW, the large acceptance of the SKS (please refer to Table I.) would make it possible to observe the $^{12}_{\Xi}$Be hypernucleus with a moderate energy resolution of 6 MeV. In fact, this was a last chance to use the SKS at the K1.8 beam line. After the E05 run, the SKS had been moved to the south area in the Hadron Experimental Hall to be used in the K1.1 beam line. Here, we summarize the specifications of the three spectrometers in Table I.

2.1 Comparison of SKS and S-2S resolving powers

Here we compare the resolving power ($\Delta p/p$) of the SKS and S-2S in the first order optics. The resolving power is exporessed as

$$\Delta p/p = \frac{\sqrt{R_{11}^2\sigma_{xin}^2 + \sigma_{xout}^2 + R_{12}^2\sigma_\theta^2}}{R_{16}} \quad (2)$$

$$= \frac{\sqrt{(1+R_{11}^2)\sigma_x^2 + R_{12}^2\sigma_\theta^2}}{R_{16}}, \quad (3)$$

where important transfer matrix elements are $R_{11} =< x|\theta >$ magnification factor in x, $R_{16} =< x|\delta >$ dispersion, and $R_{12} =< x|\theta >$. The $\theta = dx/dz$, and $\delta = (p-p_0)/p_0$, where p_0 is the central momentum. We assume position resolutions in x are same ($\sigma_{xin} = \sigma_{xout} = \sigma_x$) at the entrance and at the exit. The horizontal coordinate x_{out} is proportional to the dispersion $R_{16} \times \delta$. Then, the measurement of x_{out} with the image size of $\sigma = \sqrt{(1+R_{11}^2) \times \sigma_x^2}$ corresponds to the momentum error of σ/R_{16}.

Thus, the larger the dispersion and the smaller the magnification, we will get the better resolving power. The dispersion is proportional to the bending radius of the central trajectory ρ_0. Another important factor is R_{12}. In the point-to-point focusing, the R_{12} should be 0 by adjusting the optics parameters.

Now, in the case of E05 SKS configuration, we only had one dipole magnet SKS, so that almost no adjustable parameters to set the R_{12} as small as possible. In fact it was 0.2095 (cm/mrad.), so that the angular resolution contribution cannot be neglected. The contributions of the first and second terms in Eq. 3 are roughly 1:6.6. And also the R_{16} was fixed to be 0.549 (cm/%). As shown in Fig. 4, the focusing power of the SKS is small.

In the case of S-2S, we have a good focusing property as shown in Fig. 5. Owing to the two quadrupole magnets Q1 and Q2 at the entrance of the D1, the transport parameters are adjusted to have the $R_{12} = 0$ (cm/%) and to have a large dispersion of $R_{16} = -3.8472$ (cm/%). It should be compared with that of SKS, $R_{16} = -0.834$ (cm/%). Therefore, the dispersion ratio $R_{16}^{S-2S}/R_{16}^{SKS}$ between S-2S and SKS is enhanced to be -3.847/0.834=4.6 from the ρ_0 ratio of 3/1.83=1.64. Including the angular resolution contribution coming from the finite value of the R_{12}, assuming the σ_x=0.025 cm and the σ_θ=0.9 mrad, the resolving power of the S-2S is estimated to be

$$\Delta p/p = \frac{\sqrt{(1+0.7274^2) \times 0.025^2 + 0^2 \times 0.9^2}}{3.8472} \times 2.355 \quad (4)$$

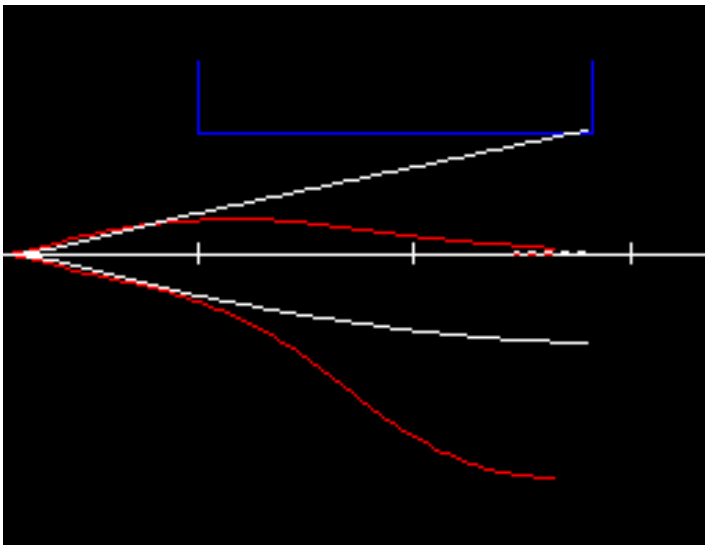

Fig. 4. A schematic transport property of the SKS. The focusing power is small.

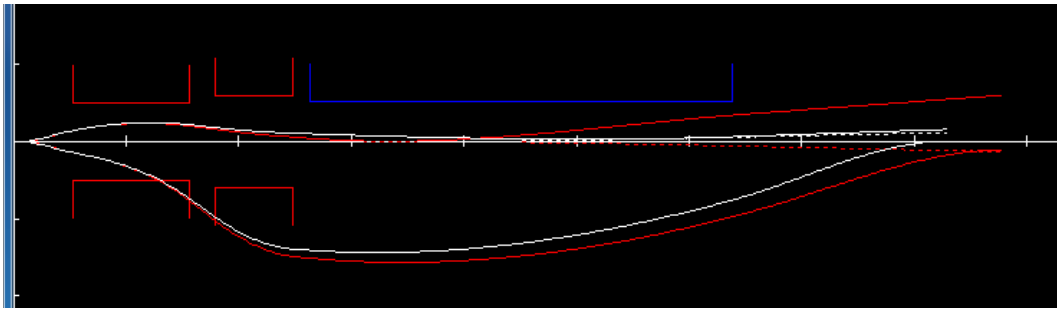

Fig. 5. A schematic transport property of the S-2S. It has a good focusing property as compared to the SKS in Fig. 4.

$$= \quad 1.9 \times 10^{-4}. \tag{5}$$

The resolving power of the SKS is

$$\Delta p/p \quad = \quad \frac{\sqrt{(1+0.549^2)\times 0.025^2 + 0.2095^2 \times 0.9^2}}{0.8339} \times 2.355 \tag{6}$$

$$= \quad 5.4 \times 10^{-3}. \tag{7}$$

Thus, from the first order optics, one order of magnitude improvement of the resolving power from the SKS to S-2S is expected.

As for the resolving power of the SKS, from the past measurements at the K1.8 beam line, we estimated it to be 3×10^{-3}, which is close to the present estimate of 5.4×10^{-3}. Since the SKS magnetic field distribution is not expressed as a simple dipole assumed in the 1st order transport, the difference in the estimations is reasonable. It was confirmed in a detailed Monte Carlo simulation taking account of the magnetic field map of SKS and multiple scattering in materials etc.

Parameters	SKS	S-2S
Bending Angle (deg.)	56.7	70
ρ_0 (m)	1.85	3
R_{16} (cm/%)	-0.834	-3.847
R_{11}	0.549	-0.727
R_{12} (cm/mrad.)	0.209	0

Table II. Comparison of optical parameters between SKS and S-2S.

3. E05 run on ^{12}C(K^-, K^+) reaction at 1.8 GeV/c with SKS

We have carried out a pilot run of the J-PARC E05 experiment at the K1.8 beam line of J-PARC hadron experimental hall, from October 26 to November 19 in 2015. The typical K^- beam intensity at 1.8 GeV/c was $6 \times 10^5 K^-$ per spill (2.2-sec. beam duration every 5.52 seconds) with a primary proton beam power of 39 kW. The K^-/π^- ratio was about 0.8. We took data using a 9.36-g/cm^2 nat-C target for about 10 days and a 9.54-g/cm^2 CH_2 target for about 2 days. The CH_2 target was used for the $p(K^-, K^+)\Xi^-$ reactions at five different incident momenta between 1.5 and 1.9 GeV/c. The total number of K^-'s irradiated on targets amounted to 100 G.

The experimental setup of the E05 pilot run is shown in Fig. 6. In the upstream part of the K1.8 beam line, we have a double-stage electrostatic separator system, and the K^- beam was finally selected through a mass slit (MS2). The incident K^- beam was defined with two sets of plastic scintillation counters (BH1 and BH2) and an aerogel Čerenkov counter (BAC) to suppress π^-'s at the on-line trigger level. The beam momentum was analyzed track by track with the tracking detectors (BFT, BC3 and BC4). The beam line spectrometer was composed of 4 quadrupole magnets (Q10-Q13) and one dipole magnet (D4). The design momentum resolution of the spectrometer was $\Delta p/p \sim 5 \times 10^{-4}$ (FWHM).

The outgoing K^+ was momentum analyzed with the SKS spectrometer with four sets of drift chambers (SDC1-4). In the pilot run, the SKS central momentum was set at about 1.3 GeV/c covering about 110 msr. The momentum resolution of the SKS was $\Delta p/p \sim 3 \times 10^{-3}$. These are great advantages of the SKS compared with the spectrometers used for the (K^-, K^+) reaction in the past.

The particles detected in the SKS were identified with a time of flight measured with a plastics scintillation counter wall of "TOF" correcting with the flight path and momentum obtained from the tracking chambers. (Fig. 7) The aerogel Čerenkov counter wall "AC" was installed to suppress pions in the trigger level, and the "Lucite Counter (LC)" for suppression of protons.

3.1 Analysis for the $p(K^-, K^+)\Xi^-$ reaction

The overall energy resolution was evaluated with the peak for the $p(K^-, K^+)\Xi^-$ reaction at 1.8 GeV/c as shown in Fig. 9, and was confirmed to be 5.4 MeV (FWHM). It is a factor of two better with respect to the 10 MeV of the BNL E885 for proton target. In the Carbon kinematics, the BNL E885 resolution was estimated to be 14 MeV, while our estimate is about 6 MeV which was dominated by the target energy loss straggling. Absolute energy scale of the (K^-, K^+) missing mass was adjusted with this peak position. About 6,000 Ξ^-'s were identified per day.

The incident momentum dependence of the forward cross sections of the $K^- + p \rightarrow K^+ + \Xi^-$ reaction was obtained at 1.5, 1.6, 1.7, 1.8 and 1.9 GeV/c. The statistics at each momentum was more than about 20 times of the statistics of the old bubble chamber data. At 1.8 GeV/c, the statistics was about 100 times to obtain the angular distribution in detail. In a preliminary analysis, we have confirmed with improved statistics that the relative strengths of the cross sections peaks at about 1.8 GeV/c (Fig. 10) as suggested by Dover and Gal [16].

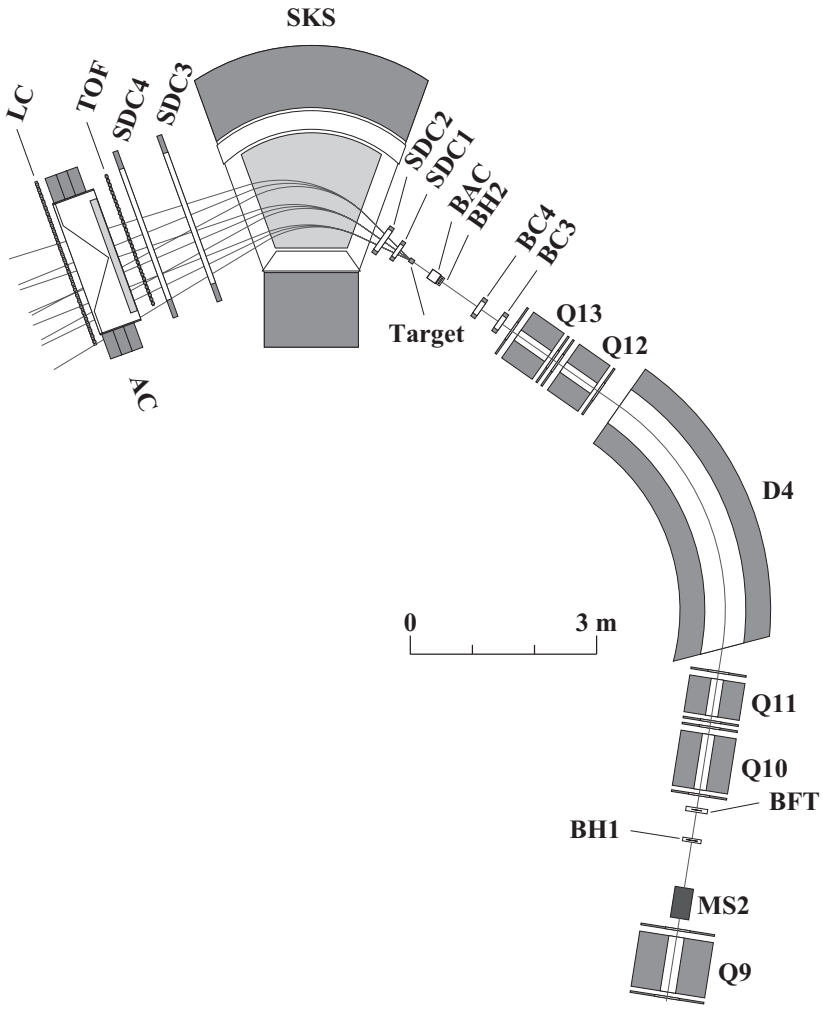

Fig. 6. A schematic view of the experimental setup during the E05 pilot run.

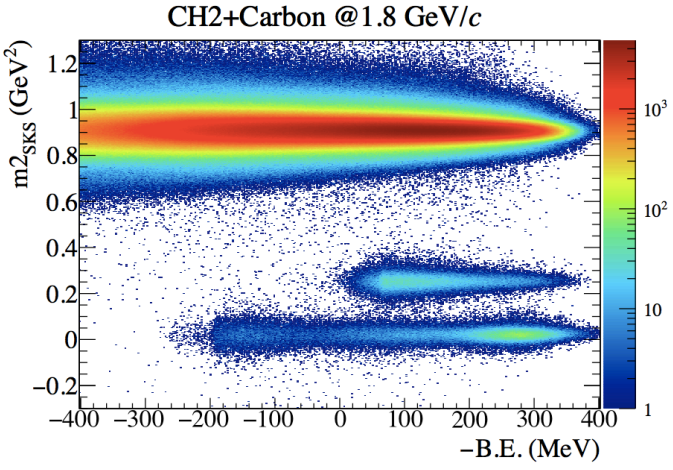

Fig. 7. Particle mass squared obtained from the TOF measurement v.s. negative Binding Energy of Ξ^- in ^{11}B.

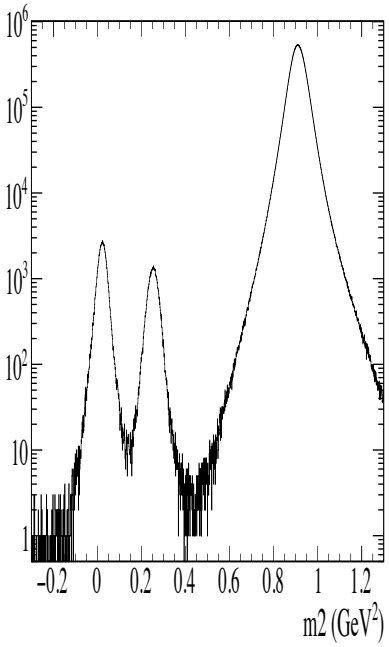

Fig. 8. Particle mass squared obtained from the TOF measurement. The Kaon peak is clearly separated in the middle of pion and proton peaks.

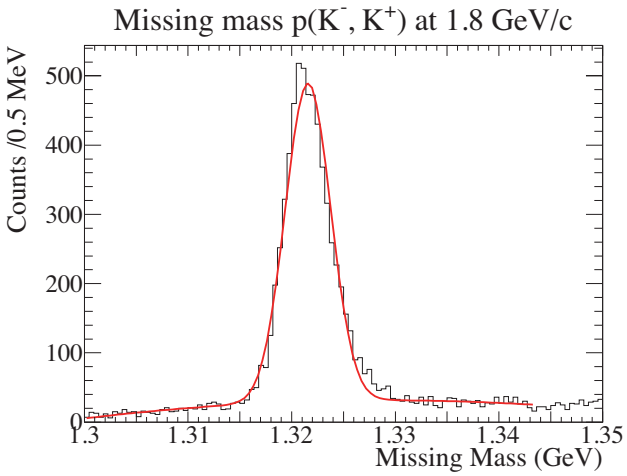

Fig. 9. Missing-mass spectrum for the $p(K^-, K^+)X$ reaction at 1.8 GeV/c obtained with a CH_2 target. The peak corresponds to the reaction on proton and the continuous background below the peak is the contribution of quasi-free Ξ production from ^{12}C.

3.2 Preliminary Analysis for the $^{12}C(K^-, K^+)$ reaction

The missing mass spectrum of the $^{12}C(K^-, K^+)$ reaction is shown in Fig. 11 as a function of negative values of binding energy (B.E.) of Ξ^- in ^{11}B. Owing to the large momentum acceptance of the SKS, we were able to obtain the spectrum in a wide energy range. The largest part of the spectrum comes from the quasi-free production of Ξ's peaking at about 100 MeV, while the contribution of Ξ^*

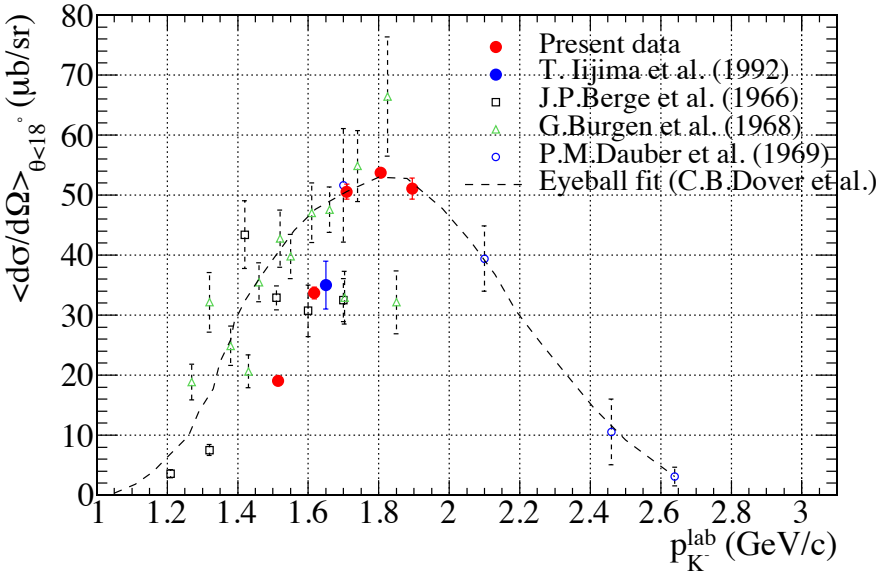

Fig. 10. The incident momentum dependence of the differential cross section of the $p(K^-, K^+)\Xi^-$ reaction at forward angles. The present data is shown in red together with other old data.

can be seen in the higher energy region. Due to the large momentum transferred to Ξ (~550 MeV/c) in this reaction, the sticking probability is small, so that there are very few events in the bound region (−B.E. <0) in this vertical scale. A large shift of the quasi-free peak is also due to the large momentum transfer.

Next we magnify the view in the bound region of Fig. 11, and we plot it in Fig. 12. Here, there should be no physical processes with a binding energy value larger than about 40 MeV (−B.E.≤ −40 MeV), where the ground state of ${}^{12}_{\Lambda\Lambda}$Be exists. Therefore, we think these events in this region should be the background, mostly coming from Kaon decay-in-flight and having almost flat distribution (5 counts/ 20 MeV). Then, we observed a significant event excess of about 50 events in the binding energy region between 0 and 20 MeV (−20 MeV≥ −B.E.≥0 MeV) shown in Fig. 12. This is the same level of statistics obtained by the BNL E885 (42-67 events). Above the binding threshold (−B.E.≥ 0 MeV), we clearly see a rise for the quasi-free production. The momentum acceptance of the SKS corresponding to this energy region is almost flat.

From the shape in the binding region, several interpretations are possible with this limited statistics and about 6 MeV energy resolution. One interpretation is that there exist a large tail reflecting a large imaginary part of the Ξ^- potential. Probably the real part of the potential would be shallow. (case (a)) However, such a large imaginary part larger than 10 MeV is not expected in Ξ hypernuclei. Another interpretation may be that there exist several bound states and the present energy resolution is not enough to resolve them. (case (b))

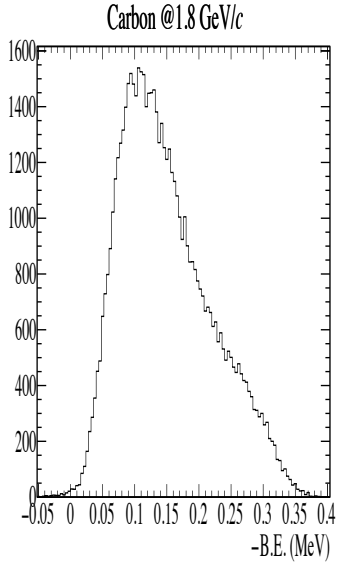

Fig. 11. Missing-mass spectra for the $^{12}\mathrm{C}(K^-, K^+)X$ reaction at 1.8 GeV/c in a wide energy range.

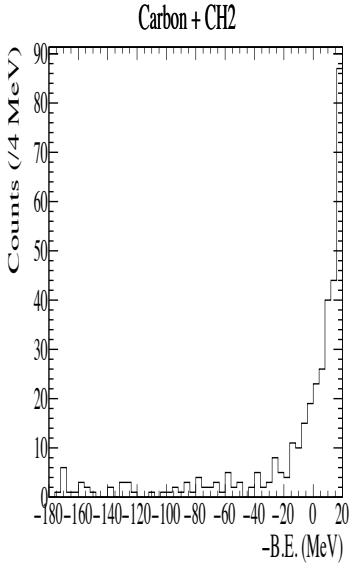

Fig. 12. Missing-mass spectra for the $^{12}\mathrm{C}(K^-, K^+)X$ reaction at 1.8 GeV/c near the binding energy threshold.

4. E70 Experimental Setup

We are going to measure a missing-mass (M_X) of the ^{12}C(K^-, K^+) reaction at 1.8 GeV/c.

$$M_X = \sqrt{(E_{K^-} + M_C - E_{K^+})^2 - p_{K^-}^2 - p_{K^+}^2 + 2p_{K^-} \cdot p_{K^+} \cos\theta}. \quad (8)$$

The incident momentum of the K^- (p_{K^-}) is measured with the K1.8 beam line spectrometer. The outgoing K^+ momentum (p_{K^+}) is measured with the S-2S spectrometer. The θ is the scattering angle between the K^- and K^+. The M_C is the mass of the target nucleus.

The K1.8 beam line spectrometer, which is shown in Fig. 6 has been used in a series of hypernuclear experiments at the K1.8 beam line. As compared with previous experimental setups for the (K^-, K^+) reaction, we have an advantage to have the beam line spectrometer system in order to achieve a good momentum resolution.

A schematic layout of the $S-2S$ spectrometer for the J-PARC E70 experiment is shown in Fig. 13. The K^- beam at 1.8 GeV/c available at the K1.8 beam line is used for the production of Ξ hypernuclei. The production yield of the Ξ^- in the $K^- + p \rightarrow K^+\Xi^-$ reaction has a maximum at 1.8 GeV/c in the forward region, which has been confirmed (Fig. 10) in the pilot run with two orders of magnitude better statistics than old bubble chamber data.

4.1 K1.8 Beam Line

In the upstream part of the K1.8 beam line, we have a double-stage electrostatic separator system, and the K^- beam was finally selected through a mass slit (MS2). The incident K^- beam was defined with two sets of plastic scintillation counters (BH1 and BH2) and an aerogel Čerenkov counter (BAC) to suppress π^-'s at the on-line trigger level.

The incident momentum is analyzed with a beam line spectrometer system composed of $QQDQQ$ in the K1.8 beam line of the J-PARC hadron experimental hall. The momentum resolution is designed to be 5×10^{-4} (FWHM).

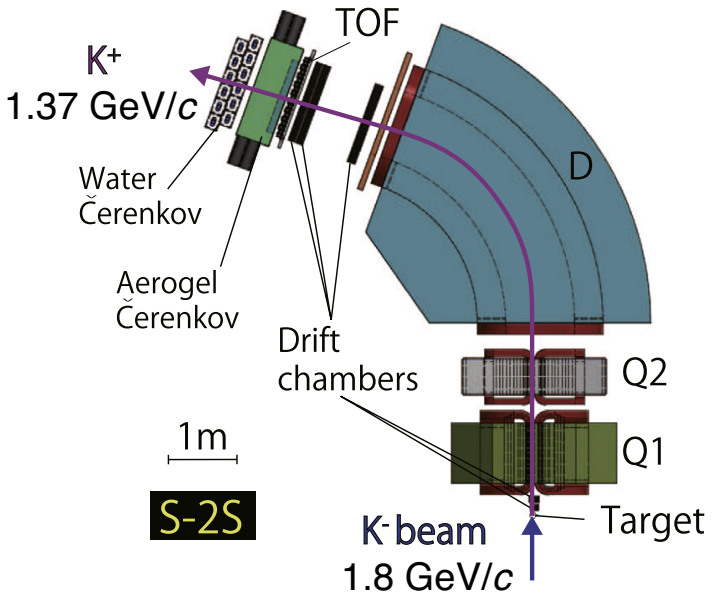

Fig. 13. Schematic view of the S-2S spectrometer system.

4.1.1 K1.8 beam line spectrometer

The beam momentum was analyzed track by track with the tracking detectors (BFT, BC3 and BC4). The beam line spectrometer was composed of 4 quadrupole magnets (Q10-Q13) and one dipole magnet (D4). The design momentum resolution of the spectrometer is $\Delta p/p \sim 5 \times 10^{-4}$ (FWHM).

4.1.2 Detectors in K1.8

We use the same detector system as used in the E05 run listed in Table III. The beam trigger counters $BH1$ and $BH2$ were used in the J-PARC E19, E27, E10 and E05. Both counters are segmented to keep the counting rate flat among the segments. They have a good time resolution of σ_t=200 ps to separate K/p. The separation between π/K was carried out with the BAC Čerenkov counter equipped with aerogels (n = 1.055).

The BFT counter consists of two layers (xx') of ϕ1-mm scintillating fiber sheets in order to handle high-intensity π beams up to $10\times10^6/s$ which was realized in the E10 measurement. The high-rate drift chambers (BDC3 and BDC4) with the drift cells of ±1.5mm are also worked well in the same condition. The typical position resolution was 250 μm (Fig. 14). The gas mixture is Ar:iso-C_4H_{10}: Methylal=76:20:4 at atmospheric pressure.

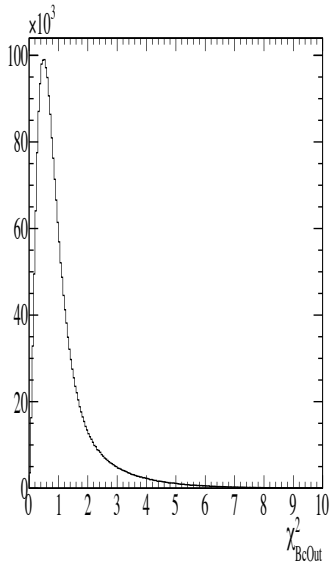

Fig. 14. χ^2 distribution of the beam line local tracking with BDC3&4.

Name	configuration	effective area (mm^2)	# of signal channels
BFT	xx'	160×80	160×2
BDC3,4	xx'uu'vv' ×2 sets	192×150	64 x 6 x 2
BH1	11 segments	170×66	11×2
BAC	2 segments	100×100 ×50	4
BH2	7 segments	145×60	7×2

Table III. Specifications of the detectors in the K1.8 beam line.

The beam line tracking through the $QQDQQ$ system is carried out by using a third-order transfer

matrix calculated with the ORBIT code.

In Fig. 15, the beam profile at a target position measured in the E05 experiment is shown. The horizontal and vertical sizes were approximately ±4 cm×±0.8 cm in FWHM (Fig. 16, 17). The vertex distribution along the beam line is shown in Fig. 18 in the E05 run.

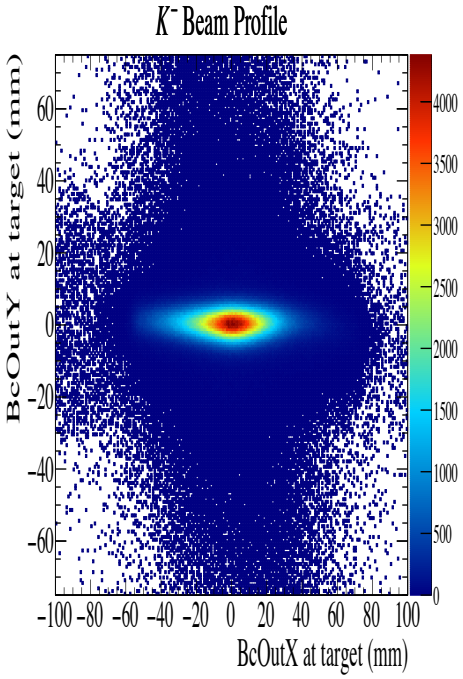

Fig. 15. K^- beam profile on a target in the E05 run at the K1.8 beam line.

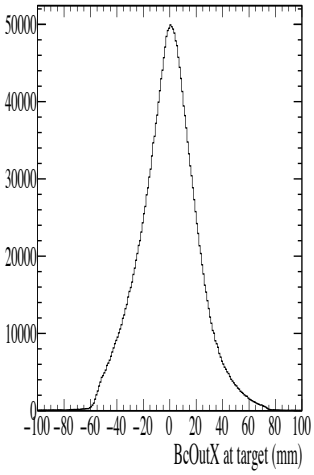

Fig. 16. K^- beam profile in X (horizontal) on a target in the E05 run at the K1.8 beam line.

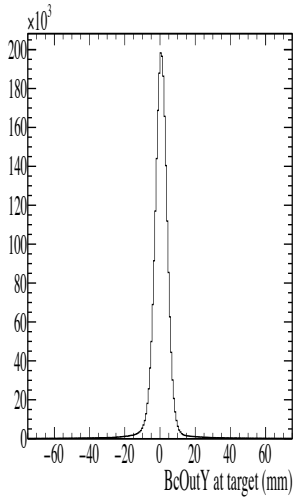

Fig. 17. K^- beam profile in Y (vertical) on a target in the E05 run at the K1.8 beam line.

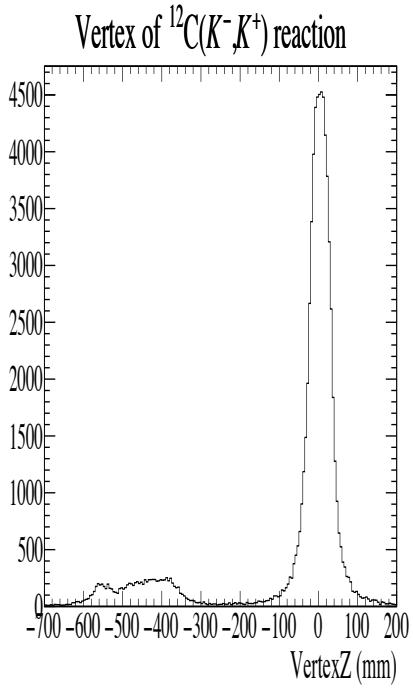

Fig. 18. The vertex distribution in the beam direction (Z) in the E05 run at the K1.8 beam line.

4.2 S-2S spectrometer

4.2.1 Magnets for the S-2S

The K^+'s scattered at forward angles of $\theta_{K^+} \lesssim 18^\circ$ from the (K^-, K^+) reaction are momentum analyzed with the S-2S spectrometer. The S-2S is composed of two quadrupole magnets and one dipole magnet (QQD). The first quadrupole magnet focuses the particles in vertical, and the next one in horizontal. A large aperture of the two quadrupole magnets keeps the solid angle as large as 55 msr as shown in Fig. 28. The bending angle for the central momentum of the dipole magnet is 70 degrees at 1.37 GeV/c. The specifications of the magnet are listed in Table IV.

	Q1	Q2		D1
Field Gradient (T/m)	8.72	5.0	Field Strength (T)	1.5
Aperture (cm)	31	36	Pole Gap (cm^2)	32×80
Weight (ton)	37	12	Weight (ton)	86
Current (A)	2500	2500		2500
Power (kW)	400	156		450

Table IV. Specifications of the magnets for the S-2S .

All the magnets were already constructed and the field distributions were measured (see Fig. 19); Q1 in March 2013, Q2 in March 2014, and D1 in May 2015. The basic performance of the magnets (Table IV) was demonstrated safely.

4.2.2 Q1

A large quadrupole magnet of the size of 2.4 m high and 2.4 m wide was constructed for the first magnet of S-2S . The length of the magnet is 88 cm. It de-focuses in horizontal and focuses in

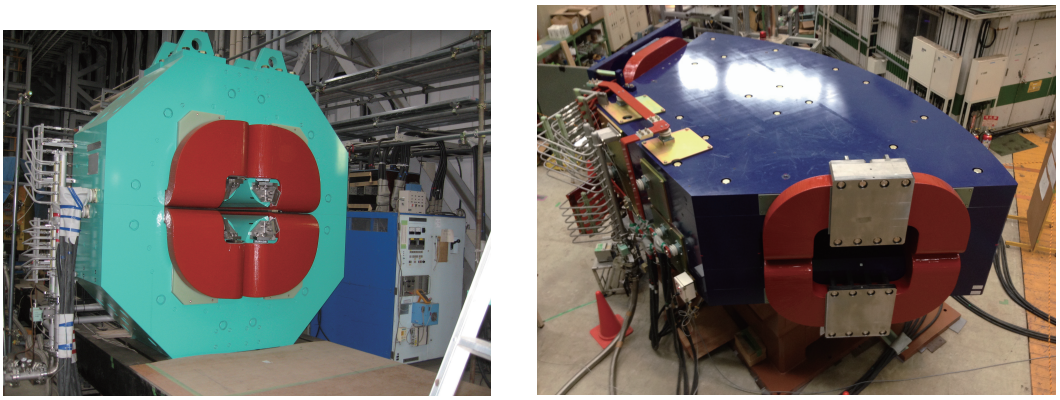

Fig. 19. Pictures of the (a) Q1 and (b) D1 magnets of the $S - 2S$ spectrometer system.

vertical. The maximum current is 2500 A with the required power of 400 kW.

The pole gap size is ϕ0.31 m.

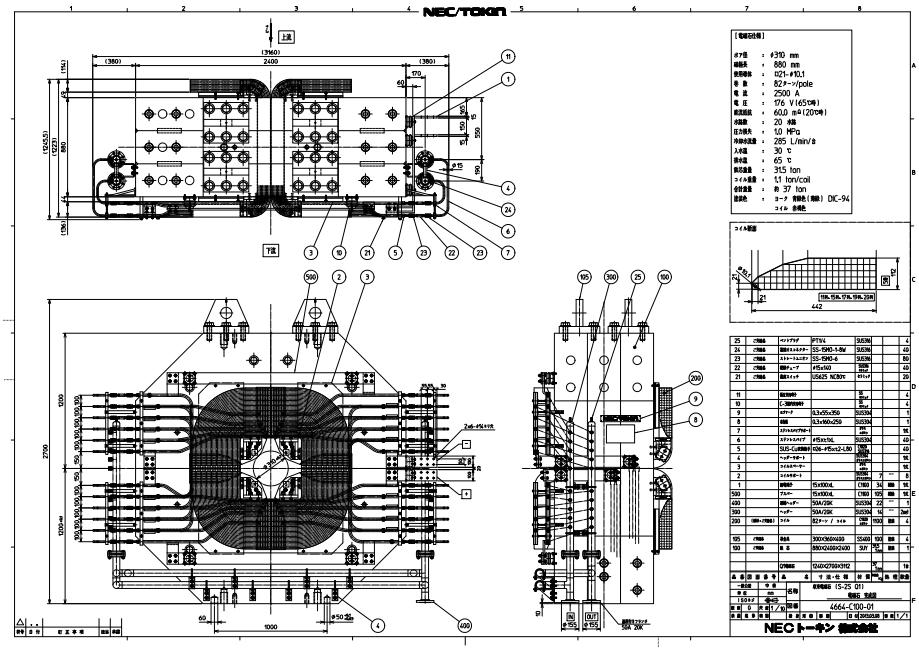

Fig. 20. A drawing of the Q1 magnet.

4.2.3 Q2

The Q2 magnet is smaller than the Q1 magnet (Fig. 23), and it focuses in horizontal and defocuses in vertical. The maximum current is 2500 A with the required power of 156 kW. A small quadrupole magnet of the size of 1.54 m high and 2.1 m wide was constructed for the second magnet

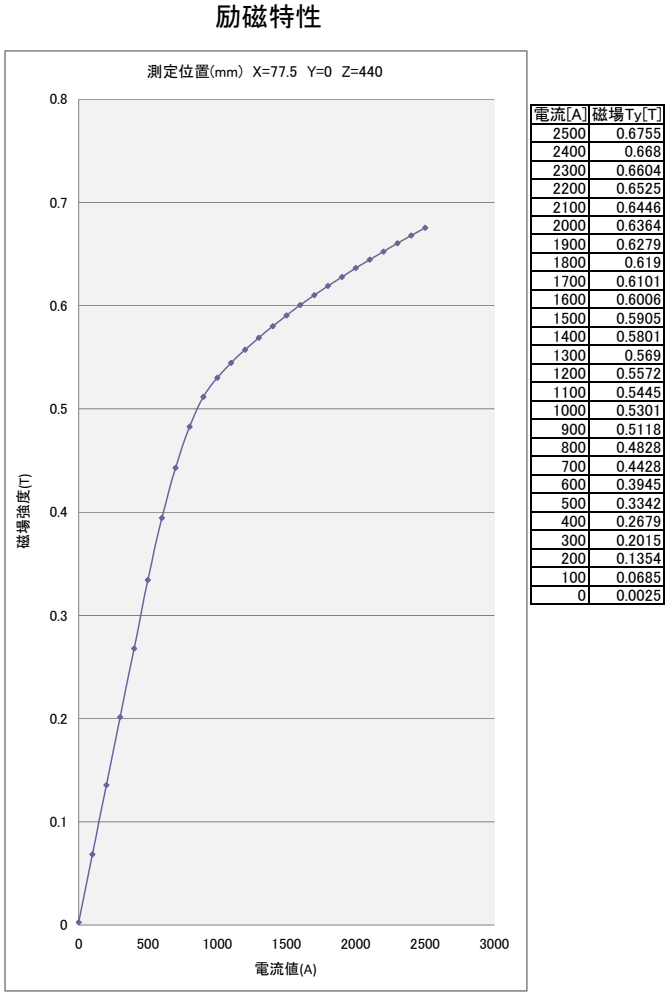

電流[A]	磁場Ty[T]
2500	0.6755
2400	0.668
2300	0.6604
2200	0.6525
2100	0.6446
2000	0.6364
1900	0.6279
1800	0.619
1700	0.6101
1600	0.6006
1500	0.5905
1400	0.5801
1300	0.569
1200	0.5572
1100	0.5445
1000	0.5301
900	0.5118
800	0.4828
700	0.4428
600	0.3945
500	0.3342
400	0.2679
300	0.2015
200	0.1354
100	0.0685
0	0.0025

Fig. 21. Excitation curve of the Q1 magnet.

of S-2S . The length of the magnet is 50 cm. The pole gap size is ϕ0.36 m. In Fig. 24, the magnetic field excitation curve as a function of the coil current is shown.

4.2.4 D1

The bending magnet $D1$ is the key magnet to have a good momentum resolution with the bending angle of 70°. The pole gap is 32 cm and the track curvature radius is 3 m. A drawing of the $D1$ magnet is shown in Fig. 25. The magnetic field strength as a function of coil current is also shown in Fig. 26.

The hysterisis of the magnet was examined for the D1 magnet. It took 10 min. to stabilize the central magnetic field with the precision of 1.6μT. Further, in setting the current, once we apply the maximum current before setting the current, the magnetic field strength reproducibility was within 0.04%, and we don't need to care about hysterisis.

The magnetic field distribution of the $D1$ magnet was measured by using a 3-dim. Hall probe in fine steps of 2 cm near the pole edges, and in rough steps of 5 cm in the magnetic field uniform region. The Hall probe was calibrated with an NMR. The errors of the magnetic field distribution were estimated with several methods: checking the Maxwell equations for magnetic field, reproducibility

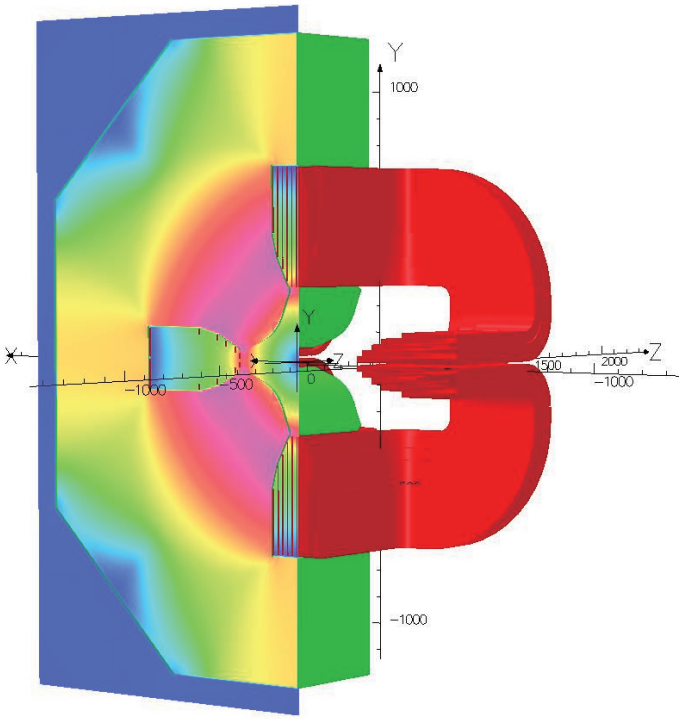

Fig. 22. Simulated magnetic-field map of the Q1 magnet of the S-2S spectrometer system.

of the magnetic field at the same position, and so on. We found the errors are within 180 μT in uniform magnetic field regions, and within 1.2 mT near the pole edge. The effect of the magnetic field measurement error on the momentum resolution was estimated with a simulation. We found the contribution was smaller than $\Delta p/p = 6\times10^{-4}$. The measured magnetic field was examined with a 3-dim. calculated magnetic field with the OPERA-3D program. We found the difference of the magnetic fields in σ was 0.4mT in uniform magnetic field regions, and within 1.3mT near the pole edges. Its effect on the momentum resolution is 5.5×10^{-4}.

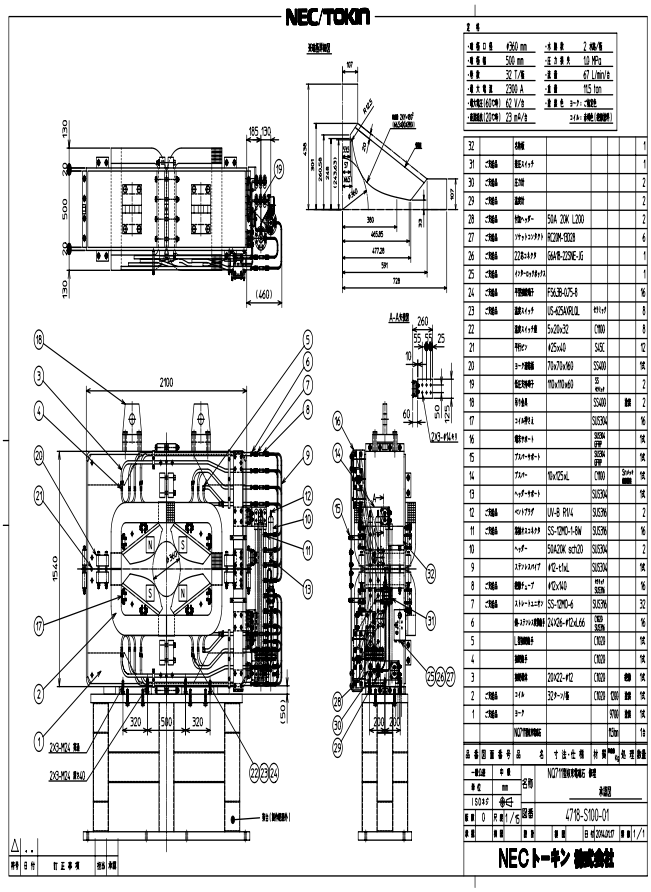

Fig. 23. A drawing of the Q2 magnet.

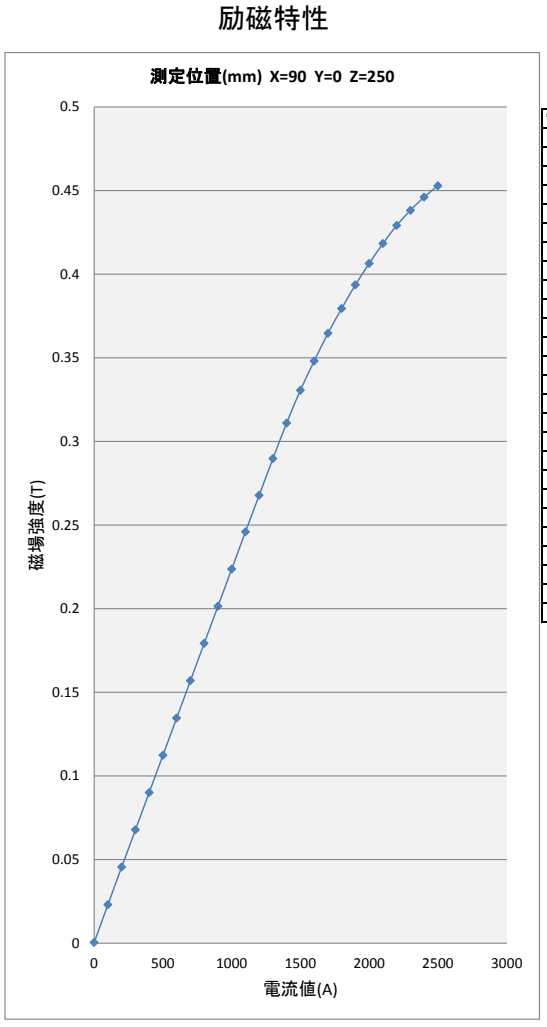

電流[A]	磁場Ty[T]
2500	0.4529
2400	0.4461
2300	0.4382
2200	0.4291
2100	0.4183
2000	0.4064
1900	0.3936
1800	0.3795
1700	0.3646
1600	0.348
1500	0.3306
1400	0.311
1300	0.2897
1200	0.2678
1100	0.2459
1000	0.2236
900	0.2014
800	0.1792
700	0.1569
600	0.1346
500	0.1123
400	0.09
300	0.0677
200	0.0455
100	0.023
0	0.0003

Fig. 24. Excitation curve of the Q2 magnet.

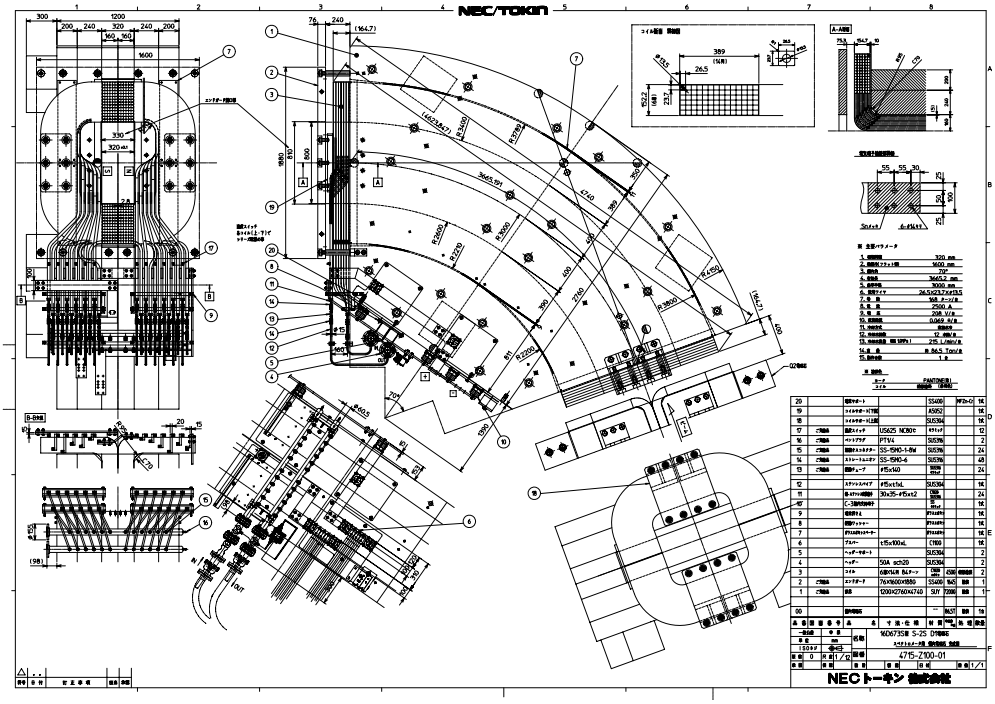

Fig. 25. A drawing of the D1 magnet.

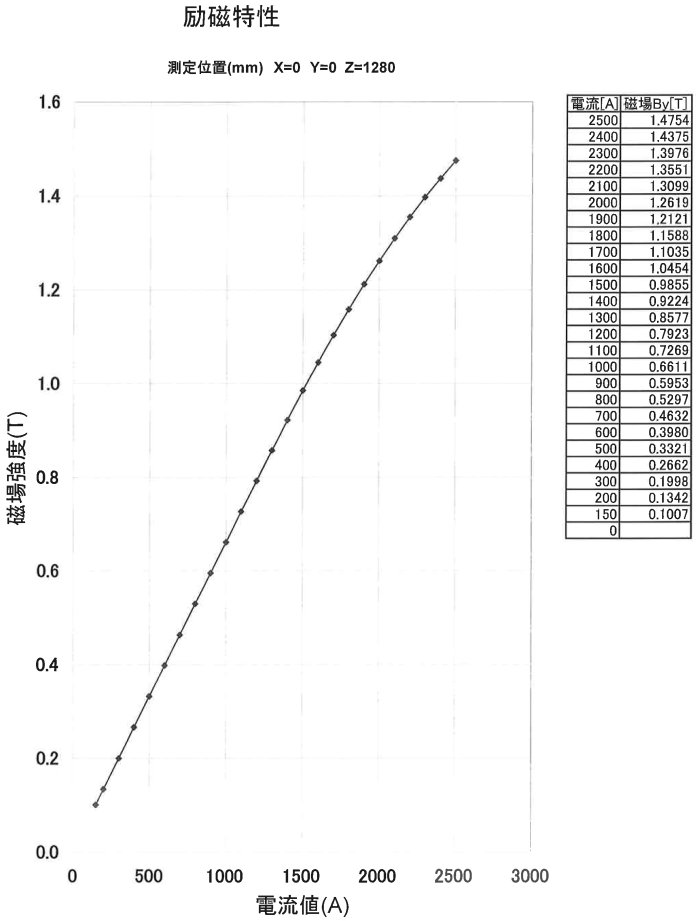

電流[A]	磁場By[T]
2500	1.4754
2400	1.4375
2300	1.3976
2200	1.3551
2100	1.3099
2000	1.2619
1900	1.2121
1800	1.1588
1700	1.1035
1600	1.0454
1500	0.9855
1400	0.9224
1300	0.8577
1200	0.7923
1100	0.7269
1000	0.6611
900	0.5953
800	0.5297
700	0.4632
600	0.3980
500	0.3321
400	0.2662
300	0.1998
200	0.1342
150	0.1007
0	

Fig. 26. Excitation curve of the D1 magnet.

4.2.5 Detectors for the S-2S

The K^+ trigger signals are generated with a time-of-flight scintillation counter (TOF), an aerogel Čerenkov counter (AC: refractive index n=1.055) for π^+ veto, and a water Čerenkov counter (WC: n=1.33) for proton veto [17], as $TOF \otimes \overline{AC} \otimes WC$. The particle identification is carried out with the TOF counter in off-line analyses by correcting the flight path and momentum obtained from the tracking in $S-2S$.

Name	configuration	effective area (mm^2)	# of signal channels
SDC1	xx'uu'vv'	394×264 × 6 planes	64 ×6
SDC2	uu'vv'	160×300 × 6 planes	44 ×4
SDC3	xx'yy'	1200×900	448
SDC4-5	xx'yy'	1200×1200	128×4
TOF	18 segments	1192×600	18×2
AC	1 box	1400×1400	30 PMTs
WC	12 segments	1450×690	12×2

Table V. Specifications of the detectors in the $S-2S$.

4.2.6 Tracking detectors

The drift chambers at the entrance of the S-$2S$ are high-rate drift chambers (SDC2) with the drift cell of ±2.5 mm. (Fig. 27). The gas mixture is Ar:iso-C_4H_{10}: Methylal=76:20:4 at atmospheric pressure.

We have three sets of drift chambers at the exit of the S-$2S$. The gas mixture used is Ar: C_2H_6 = 50:50.

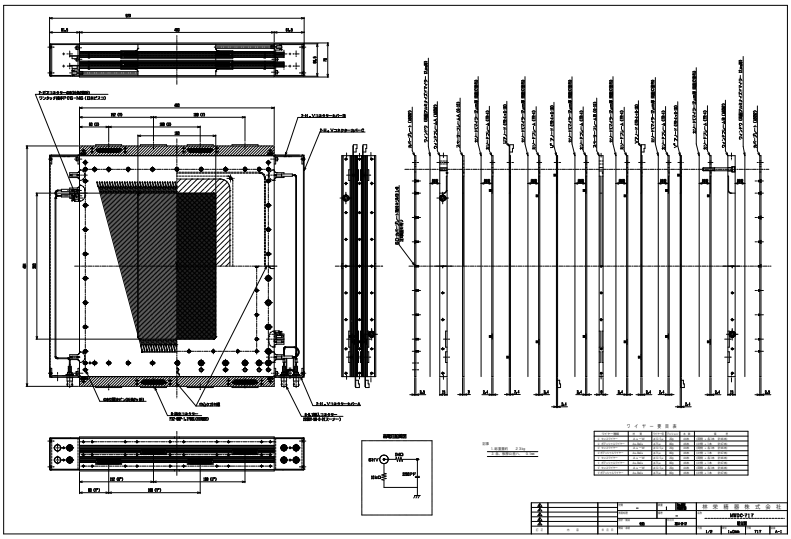

Fig. 27. A drawing of the SDC2 chamber.

The momentum acceptance of the S-$2S$ ranges from 1.2 to 1.6 GeV/c with the solid angle acceptance larger than ~20 msr. The K^+'s decay in fight, so that the flight length is kept as short as 9 m

with a survival rate of 40%.

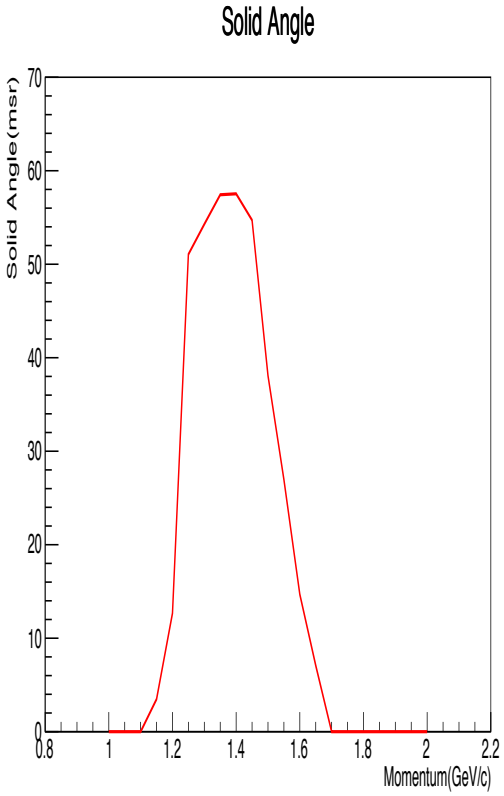

Fig. 28. Acceptance of the S-2S spectrometer as a function of momentum. The momentum for the $\Xi-$hypernuclei bound states production corresponds to ~1.37 GeV/c.

The momentum resolution of the S-2S is estimated from a simulation and found to be 5.5 $\times$ 10^{-4} (FWHM) by assuming the position resolution of drift chambers to be 250 μm(Fig. 29). It is necessary to fill all the space in between the tracking chambers with ^{4}He gas to reduce multiple scattering effects for the momentum resolution. The S-2S spectrometer is a similar spectrometer with the HKS constructed at JLab [18]. The momentum resolution was realized to be 2×10^{-4} (FWHM) at 1.2 GeV/c. Due to a large background in front of the HKS, they did not have any tracking detectors in the front section. Thus they needed careful calibrations putting a sieve slit collimator to limit the trajectories. In the case of S-2S, we have tracking detectors in front of the S-2S. So, we don't need this calibration.

In order to analyze the K^+ momentum, the magnetic-field map of the S-2S system is necessary. Since the magnetic field measurement with three magnets in their regular positions is difficult, we have measured the field map for each magnet separately. These measured field maps are compared with the calculated field maps by using a three-dimensional finite-element method Opera3D/TOSCA. By optimizing the B-H curve for the irons, we have succeeded to reproduce the Q1 magnetic field within an accuracy of $\pm$20 Gauss (Fig. 22). Reproducing the field map of each magnet, the field map of the three-magnet system will be calculated with the same code by placing all the three magnets. Of course, this will be a starting point of the field map to be used for momentum analyses in the S-2S . We need to optimize the field map by using the $K^- + p \rightarrow K^+ + \Xi^-$ events as the calibration source.

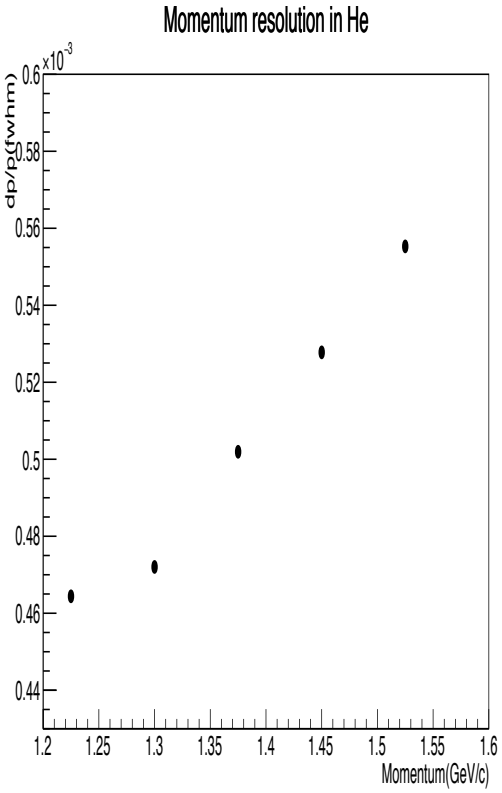

Fig. 29. Momentum resolution of the S-2S spectrometer in FWHM assuming that the position resolution of the tracking detectors are 250 μm in r.m.s. as a function of momentum.

4.2.7 Trigger detectors

The TOF wall covers 1.2 m×0.6 m with 18 segments of plastic scintillator having a time resolution better than 200 ps. The TOF wall has been purchased already. A schematic drawing is shown in Fig. 30 (LEFT), together with a drawing for Water Čerenkov counter. The WC covers 1.45 m×0.69 m with 12 segments. It suppresses proton counts by 95%. They were developed at Kyoto University and almost ready for installation. The AC counter is used for pion suppression with an efficiency of more than 99% covering 1.4 m× 1.4 m. This AC has been used for the SKS for a long time.

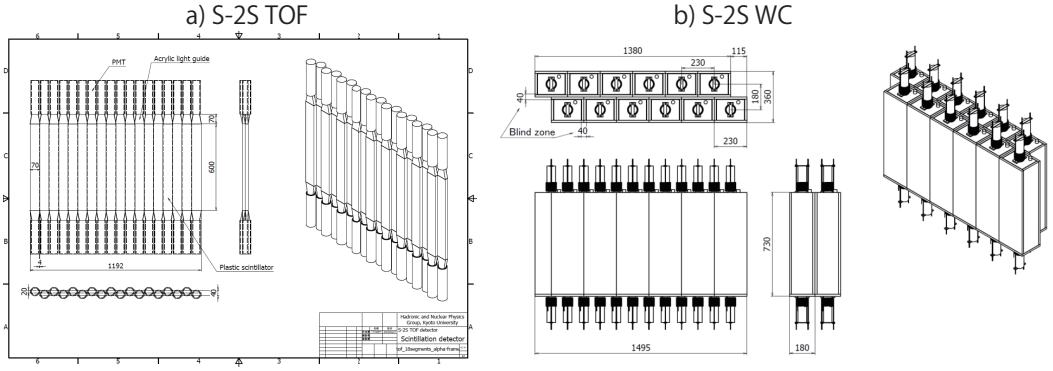

Fig. 30. Schematic drawings of the TOF and WC counter walls for S-2S .

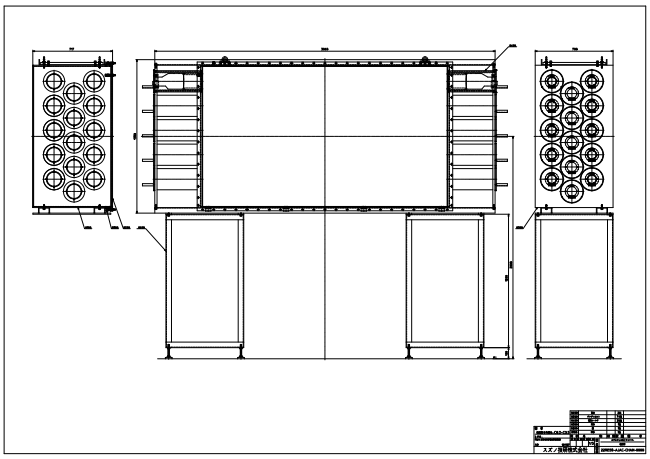

Fig. 31. Schematic drawings of the AC counter walls for S-2S .

The ”KAON” triggers in the E05 data taking was less than 2000 triggers/spill from the 9.3-g/cm^2 target. In E70 the target thickness is almost the same, spectrometer acceptance will be reduced by half (55 msr/110 msr), and the beam intensity will be doubled by doubling the primary proton beam power (80 kW / 39 kW). Therefore same level of triggers are expected when no improvements of trigger. The triggers are pi:p=1:1 = 500 : 500. We will install the WC, so that proton counts be reduced by 1/10=50, and the pion counts will be 1/100 =5. So, in total, 55 counts/spill. In this trigger rate, our DAQ system has an efficiency of 95%.

4.3 Active Fiber Target (AFT)

We will use a 9 g/cm^2 thick target of fiber scintillators. A dimension of the target will be $5^H \times 10^W \times 10^T$ cm^3 consisting of ϕ3 mm scintillating fibers (Saint-Gobain, ®BCF-10SC). In Fig. 15, the beam profile observed in E05 experiment which was carried out in 2015 is plotted. The fiber target is designed to cover the beam area. One unit of the fiber target is composed of four planes (xx'yy') of 100 fibers, and there will be nine units along the beam direction using 900 fibers in total (Fig. 32). A net thickness of AFT is almost the same as that used for the E05 experiment.

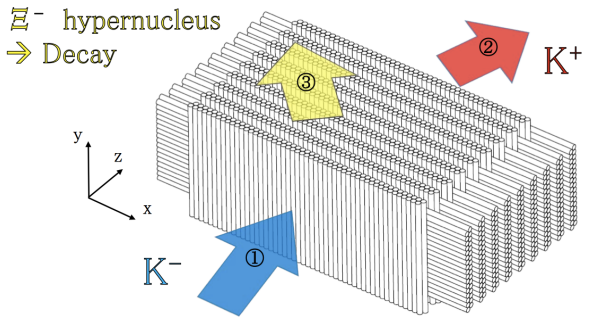

Fig. 32. A conceptual design of the active target made of ϕ3 mm scintillation fibers.

In the E05 experiment, an energy resolution in a resulting missing mass spectrum is estimated to be about 6 MeV to which an energy straggling in the target largely contributed. Scintillating light in the fiber will be converted to photoelectrons by MPPC, and electric signals due to photoelectrons will be read by EASIROC. The output signal strength correlates with the number of photons generated in the fiber, which actually corresponds to the energy loss in the fiber. Therefore, the signal strength which will be recorded as ADC can be used for a correction of the energy straggling event by event when the missing mass is reconstructed. An introduction of the active fiber target (AFT) is expected to lead to the energy resolution as good as about 2 MeV (FWHM) for the Ξ-hypernucleus measurement maintaining a fairly thick target thickness.

A total flight length of a particle in an active volume of fiber is shown in Fig. 33. The fiber has a clad with a 3% of the outer diameter for light transmission, and the clad is inactive for scintillation. On average, a particle passes through about 84% of the total flight length in the active scintillation volume.

A test to check basic performance of our scintillating fiber system was done at RCNP, and a result is shown in Sec. 4.3.1. We have a plan of further test at ELPH in 2019 as described in Sec. 4.3.2. Sec. 4.3.3 shows a rough schedule of the AFT construction and commissioning. The following subsections show how we will use AFT to correct energy straggling event by event for a missing mass calculation.

4.3.1 Energy Resolution test at RCNP

The expected energy loss of kaons in E70 is about ΔE = 0.7 MeV in ϕ3 mm fiber. In order to measure an energy resolution of the fiber at about ΔE = 0.7 MeV, we performed beam tests at RCNP, Osaka University in June and December, 2016. The Grand Raiden Spectrometer was used to measure the energy loss in each fiber for a beam particle by particle. The momentum resolution of the Grand Raiden is 1/37000 FWHM, and the resolution is good enough to see the energy resolution of a fiber. Protons at 65 and 245 MeV with a rate of 12 kHz were incident on the fiber in the experiments.

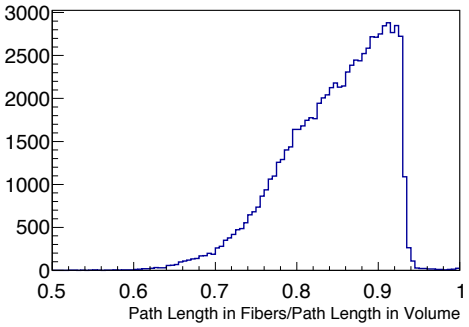

Fig. 33. Flight length distributions of a K^-. About 84% of the volumes are active scintillator parts.

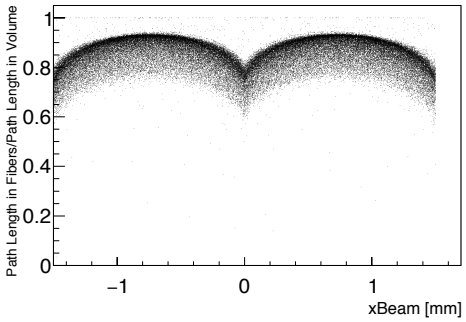

Fig. 34. Flight length distribution for a K^-. The horizontal position was distributed in ±1.5 mm (in one fiber). It depends on the incident position of the active target.

Typical energy losses in the ϕ3 mm fiber were 3 and 0.7 MeV at the proton energies of E_p = 65 and 245 MeV, respectively . A typical light output was about 650 photoelectrons at E_p = 65 MeV. A top panel of Fig. 35 shows the beam energy spread measured with the Grand Raiden spectrometer. The beam lost its energy in the fiber when we installed the fiber in front of the spectrometer as the second panel of Fig. 35 shows. When we applied an energy correction by using light output of the fiber, the beam energy could be corrected to be the original value (at zero) as shown in the bottom panel of Fig. 35 though the distribution was broadened due to the energy resolution. We obtained a ΔE dependence of the energy resolution. As a result, it was found that the energy resolution of the fiber is $\Delta E/E$ = 10% at ΔE = 0.7 MeV which corresponds to a mean value of energy loss of kaons in E70. We performed a Monte Carlo simulation in which the obtained energy resolution of the fiber was taken into account to estimate an overall missing mass resolution. As a result, it was found that AFT allows us to achieve better than 2-MeV/c^2 FWHM resolution for hypernuclear missing mass with a 9-g/cm^2 thick target.

4.3.2 Test of multi-channel readout at ELPH

A few of fibers were used in the RCNP test that was described in the previous sub-section. However, more than 900 channels of AFT are to be operated in E70 experiment. The multi-channel read out using MPPC combined with EASIROC under a high rate (2M counts/spill with 5000 channels of scintillating fibers) has already been established in J-PARC E40 experiment. Although, for AFT, we will use the same equipment and DAQ as those in E40, the multi-channel readout of AFT needs to be tested with our system prior to the experiment. We submitted the beam test proposal to the ELPH PAC in Jan 2019. We will assemble three units (xxyy (100 ch) 3 2 (two edge read-out) = 600 ch) and will use it for the test. The test will be carried out at the GeV-gamma experimental room at ELPH, and E70 AFT will be exposed to 800-MeV/c positrons with a beam rate from a few kH to a few hundred kHz. We will install two layers of particle trackers that consists of 1 mm fiber scintillators so that particle tracks can be reconstructed in an analysis. The tracking information will be used to investigate (1) position and (2) angular dependence of light output, and (3) cross talks among readout channels. (4) The variations of light output and efficiency depending on a readout channel will also be investigated.

4.3.3 AFT construction and commissioning schedule

The test at ELPH is planned to be done in June 2019 with three units of AFT. Rest of six units will be assembled through July to November, followed by a whole system test with cosmic rays. We

will propose to have another test experiment at ELPH in November or December, 2019 if needed. In addition, we are proposing to have an AFT test using the $p(K^-, K^+)\Xi^-$ reaction during the next experiment, which would be E03 experiment (using KURAMA spectrometer), at K1.8 beamline in January 2019. Yield of $p(K^-, K^+)\Xi^-$ was 210 counts/h with a 3-g/cm^2 polyethylene target at 300k K^- /spill, and an achieved resolution was about 20 MeV (FWHM) in E07 experiment in which KURAMA was used. We request eight hours beam time on AFT to collect more than 8000 events with 500k K^- /spill so that we can suppress statistical uncertainty to be about 0.1 MeV for Ξ^- peak center measurement with the 20-MeV FWHM resolution. In addition, we request beam time of four hours for AFT commissioning. Thus, in total, we request beam time of twelve hours for the test ($p(K^-, K^+)\Xi^-$ measurement and commissioning). The analysis method to correct kaon energy loss in AFT will be applied for the Ξ production along with a pattern recognition to distinguish kaons from background particles which are originated from Ξ decay. The AFT analysis algorithm which is developed in the Monte Carlo simulation will be optimized with these real data. In addition, we request to install and test AFT being exposed to scattered particles at the most downstream of a spectrometer (KURAMA in the case of E03) during the next beam time at K1.8 beamline. These data will allow us to perform gain matching, to test long term stability and so on.

4.4 Energy-loss correction in AFT

In the following subsections, we describe how we use the active target in E70.

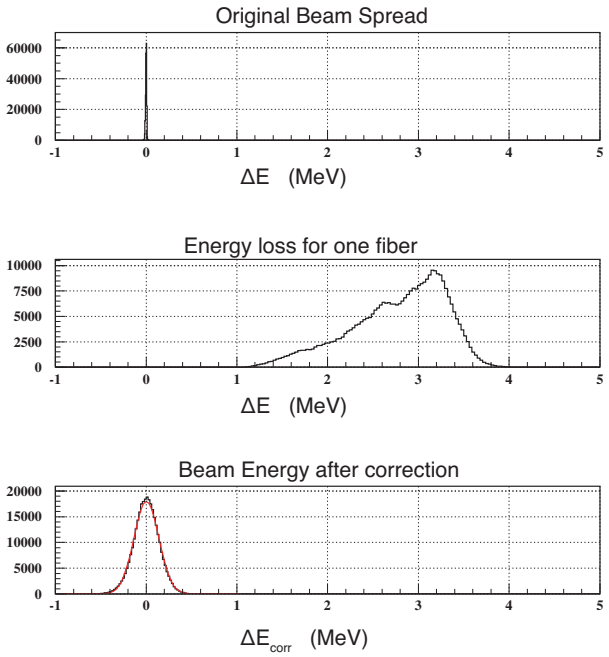

Fig. 35. Results of the RCNP test run for the fiber scintillator. Top) Beam energy spread of 65-MeV proton beam, Middle) Energy loss distribution measured with the Grand Raiden spectrometer for a ϕ3 mm scintillating fiber (Widely distributed due to energy loss position dependence and straggling.), Bottom) After correction by using the fiber light output, the width gets narrower.

4.4.1 K^- beam through

First, by using the K^- beam, we can calibrate the gain of each fiber output. The beam will be irradiated on a wide range of the target volume. In one hour 1000 triggers/spill × 600 spills/hour, we can obtain about 6000 counts/fiber, which is enough for the gain calibration. We have an option to use low momentum proton beams to calibrate with other β particles.

For these K tracks, Fig. 33 shows how much of the track is covered by an active scintillation material; about 84% are covered. It depends on the incident position as shown in Fig. 34.

From this calibration, we will obtain a function which converts the number of photo-electrons ($N_{p.e.}$) to energy deposit (ΔE), $\Delta E(i, j, k; N_{p.e.})$, i=1,70, j=1, 34, k=1, 9).

The energy-loss correction for the (K^-, K^+) missing mass measurement is done after identifying the reaction vertex as the energy deposit maximum , say ($i_{max}, j_{max}, k_{max}$). The energy of the K^- is

$$E_{K^-} - \sum_{i=1,i_{max-1},j=1,j_{max-1},k=1,k_{max-1}} \Delta E - \Delta E^K_{max}$$

, while the energy of the K^+ is

$$E_{K^+} + \sum_{i=i_{max-1},i_{end},j=j_{max+1},j_{end},k=k_{max+1},k_{end}} \Delta E + \Delta E^K_{max}$$

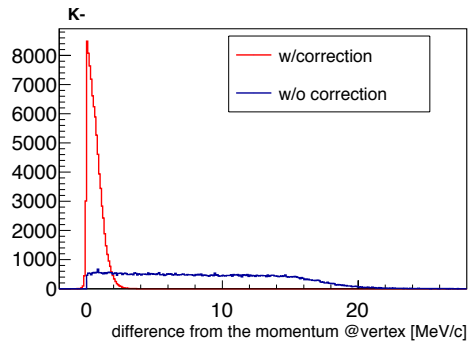

Fig. 36. K^- momentum distribution before and after the correcction.

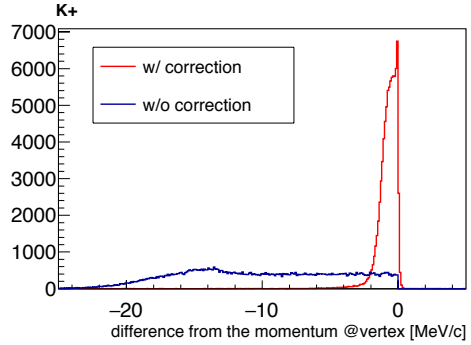

Fig. 37. K^+ momentum distribution before and after the correcction.

4.4.2 $K^-p \to \Xi^- K^+$ reaction

In the elementary Ξ^- production reaction, we have a Ξ^- and a proton in the final state. The production of Ξ^- takes place one of the fibers (we call it the production fiber.) The Ξ^- decays in flight with a recoil momentum of 550 MeV/c. wlthin the life time ($c\tau$=4.91 cm) the Ξ^- decays by emitting a π^-; about 1/8 in the same fiber, and 7/8 in the other fiber nearby. In both cases, the energy deposit in the production fiber (ΔE^{prod}) exceeds that for the K^- beam through.

A typical event pattern for the elementary Ξ^- production to be observed in the active target is shown in Fig. 38.

In Fig. 39, the missing mass distributions of the elementary Ξ^- production events before and after the energy loss corrections are shown. The missing mass resolution is improved from 2.9 MeV(FWHM) to 1.3 MeV(FWHM).

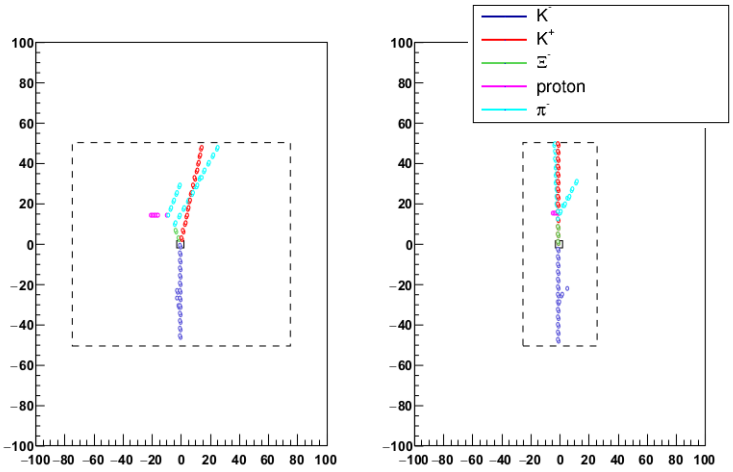

Fig. 38. A typical event pattern for the elementary Ξ production event.

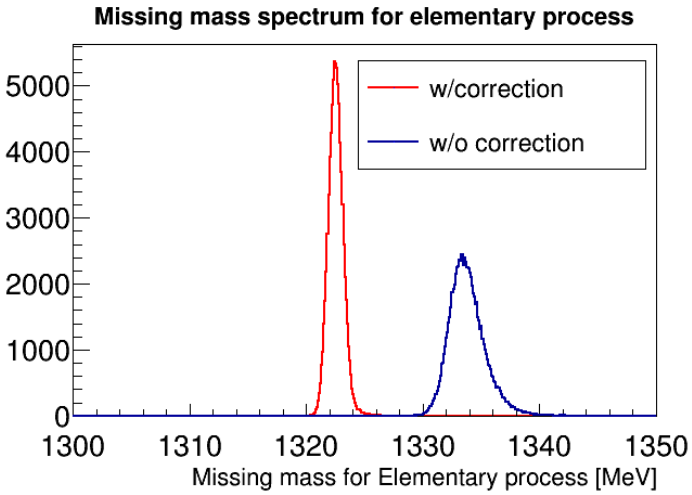

Fig. 39. Missing mass distributions for elementary Ξ^- production before and after the energy loss corrections, taking account of the momentum resolution of the spectrometers.

4.4.3 ${}^{12}_{\Xi}Be \rightarrow {}^{10}Be + \Lambda + \Lambda$

Next we consider the case where a Ξ hypernucleus is produced and decays by emitting two Λs in continuum. A typical event pattern to be observed in the active target is shown in Fig. 40. About 1/3 of Λ's decay in the production fiber, and a nuclear recoil deposits a large energy. A Λ decays into a proton and a π^- with the branching ratio of about 2/3, and other 1/3 into a neutron and a π^0; no charged particles. Therefore, with the probability of 1/9, no charged particles are accompanied. With 4/9, one Λ is accompanied, and another 4/9, two Λs. The production point is identified with a large energy deposit of the recoil nucleus ^{10}Be. The protons from the Λ decays have low betas and identified with large energy deposits as shown in Fig. 41. They are separated from the beam and scattered Kaons. The 95% of the energy deposits of more than 1.5 MeV correspond to the hits from the decay Λ's and a recoil nucleus. So by rejecting these high energy deposit fibers, we can select the

energy deposit of K's.

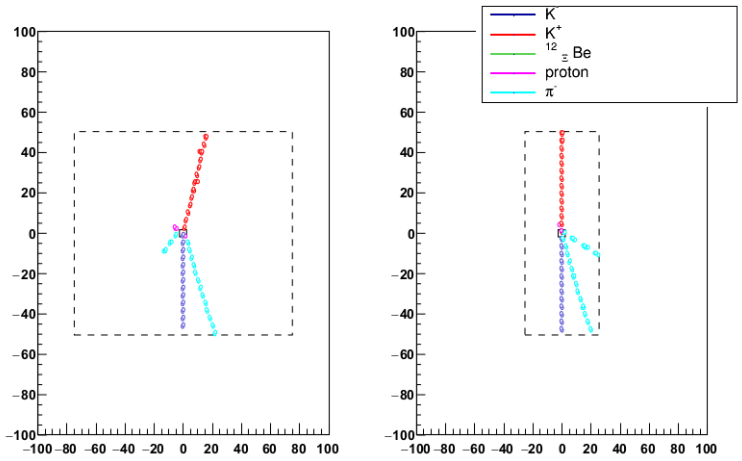

Fig. 40. A typical event pattern for the Ξ hypernuclear production event.

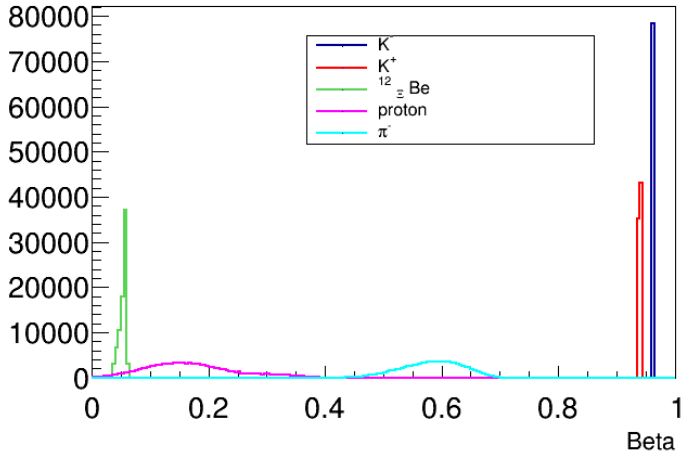

Fig. 41. The velocity β distributions in the Ξ hypernucleus production events, including the decay products (pion and proton).

In Fig. 42, the missing mass distributions of these hypernuclear events before and after the energy loss corrections, taking account of the momentum resolution of the spectrometers, are shown. The missing mass resolution is improved from 4.1 MeV(FWHM) to 2 MeV(FWHM).

4.5 DAQ, Electronics and Triggers

DAQ system and components in E70 will be almost same as those used for present experiments in K1.8 Beamline. A schematic view of the DAQ system is shown in Fig. 4.5.

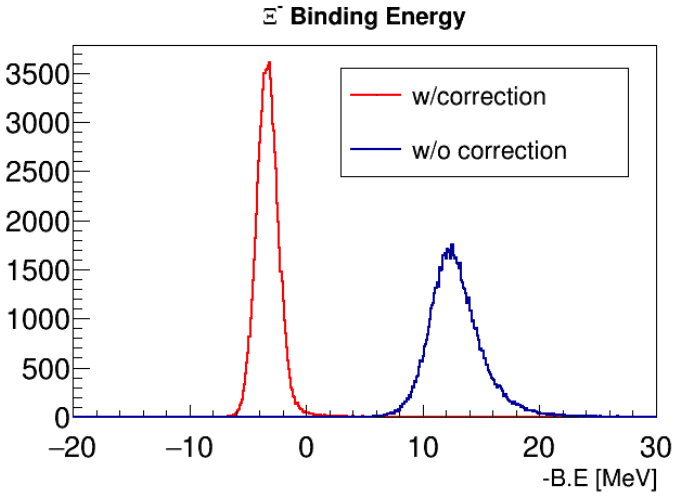

Fig. 42. Missing mass distributions for hypernuclear production before and after the energy loss corrections, taking account of the momentum resolution of the spectrometers.

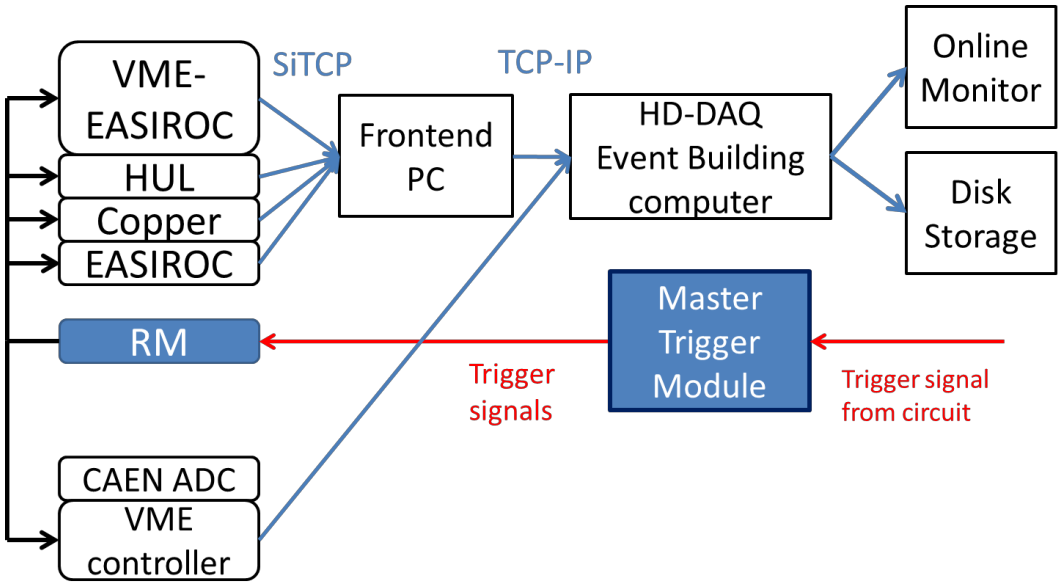

Fig. 43. Schematic view of DAQ system of E70

Modules used in E40 (2018.6) and E70 are compared in Table 4.5.

In E40 experiments, DAQ efficiency was examined changing trigger rate. 98.3 % DAQ efficiency was achieved in condition with 1300 counts/spill Level1 trigger rate and 95.7 % DAQ efficiency was achieved even in condition with 3000 counts/spill Level1 trigger rate. From this result, we can conclude DAQ system has enough capability for E70 experiment in which estimated trigger rate is less than 1000 counts/spill.

Table VI. List of readout modules which will be used in E70.

standard	detector	device	channels	TDC	ADC	Remarks
Copper-lite						
	BC3, BC4, SDC1	Chamber	384 ×3	Finesse TDC	None	
VME						
	BH1,2, TOF	PMT	22+14 +36	HUL-HR TDC	CAEN V775	E40 86 ch
	BAC, AC,WC	PMT	4+30 +24	HUL TDC	CAEN V775	E40 4 ch
	SDC2, 3, 4, 5	Chamber	176+448+512+512	HUL-MH TDC	None	E40 832 ch
	AFT	MPPC	~2000	VME-EASIROC	VME-EASIROC	E40 CFT:~5000 c
Other						
	BFT	MPPC	320	EASIROC-Board	None	

Conditions	$\left(\frac{\partial M}{\partial p_{K^-}}\right)\Delta p_{K^-}$	$\left(\frac{\partial M}{\partial p_{K^+}}\right)\Delta p_{K^+}$	$\left(\frac{\partial M}{\partial \theta_{KK}}\right)\Delta\theta_{KK}$	$\Delta E_{straggle}$ (thickness)	ΔM
Designed	0.84 MeV	0.62 MeV	0.04 MeV	1 MeV (3 g/cm^2)	1.45 MeV
Next run (Active)	1.67 MeV	0.62 MeV	0.04 MeV	0.9 MeV (10 g/cm^2)	2 MeV
Next run (Normal)	1.67 MeV	0.62 MeV	0.04 MeV	2.4 MeV (8 g/cm^2)	3 MeV
E05 Pilot run	1.67 MeV	3.74 MeV	0.04 MeV	3 MeV (10 g/cm^2)	5.1 MeV

Table VII. Contribution of each term for the missing-mass resolution in each run condition. Top) Design goal of the S-2S assuming the beam line spectrometer has $\Delta p/p = 5 \times 10^{-4}$, 2nd) Next E70 run with an active target, 3rd) Next E70 run with a normal target without target energy-loss correction, and Bottom) An estimate for the E05 pilot run.

5. Overall Energy Resolution

The hypernuclear missing-mass, M_Ξ, is defined as

$$M_\Xi = \sqrt{(E_{K^-} + M_A - E_{K^+})^2 - p_{K^-}^2 - p_{K^+}^2 + 2p_{K^-} \cdot p_{K^+} \cos\theta}. \tag{9}$$

From this equation, the missing-mass resolution is expressed with the measurement errors of Δp_{K^-}, Δp_{K^+}, and $\Delta\theta_{KK}$, as

$$\Delta M_\Xi^2 = \left(\frac{\partial M}{\partial p_{K^-}}\right)^2 \Delta p_{K^-}^2 + \left(\frac{\partial M}{\partial p_{K^+}}\right)^2 \Delta p_{K^+}^2 + \left(\frac{\partial M}{\partial \theta_{KK}}\right)^2 \Delta\theta_{KK}^2 + \Delta E_{straggle}^2, \tag{10}$$

where the $\Delta E_{straggle}$ is the error due to the energy-loss straggling in the target. The contribution of each term and the missing-mass resolution with a specific target thickness is listed in Table VII. Here, the momentum resolution of the K1.8 beam line spectrometer is assumed to be 5×10^{-4} in the "Designed" column, while it is assumed to be 1×10^{-3} in other run conditions, which was estimated in the K1.8 experiments with SKS. Please note the momentum resolution of the SKS in the previous J-PARC experiments was 3×10^{-3} so that the overall momentum resolution be limited by the SKS resolution. Therefore, we hope to achieve much better momentum resolution close to the design value of 5×10^{-4} for the K1.8 beam line spectrometer calibrated with the S-2S . In the Table VII, we used 1×10^{-3} conservatively for the next runs.

Here, we also summarize the performance of the three spectrometers with reference to the design values.

5.1 Construction status of the S-2S Spectrometer and Construction plan

K1.8 The K1.8 beam line is used for the K^- beam, and all the detectors which are common to use this beam line are ready at J-PARC. Since the K^- beam intensity is significantly smaller than π^-,

$\Delta p/p$	1st order optics	Measured	Design Value
SKS	5.4×10^{-3}	3×10^{-3}	—
S-2S	1.9×10^{-4}	—	5×10^{-4}
Beam line	4×10^{-4}	1×10^{-3}	5×10^{-4}

Table VIII. Momentum resolutions are compare with SKS, S-2S, and K1.8 beam line spectrometer. As discussed in the text, the measured momentum resolution of the beam line spectrometer is about twice of the design value.

there will be no problem for high-rate operations.

QQD The QQD magnet system for S-2S including the magnet basement is ready for moving from Tsukuba to J-PARC.

SDC1-2 Two SDCs are already in J-PARC. We will construct a mounting frame at the entrance of the Q1 magnet.

SDC3-5 Chambers are at J-PARC. We need to develop the ASD cards for these chambers. Also we need the mounting frame for these chambers during the summer in 2019.

TOF The new TOF wall is constructed together with the frame stand (Fig. 30). The last item to be consider is the magnetic field shield for PMTs, which will be purchased in January to March in 2019.

AC The aerogel counter is ready for installation at J-PARC. We will purchase 100-200 pieces of aerogel for maintenance. The aerogel Čerenkov detector is expected to reject π^+'s more than 99.7%.

WC We have developed a water Čerenkov detector for the $S-2S$ to reduce the proton trigger background by one order of magnitude. We need to construct a frame stand in the spring of 2019.

Active Target We will fabricate the three sets of (xx'yy') layers of the active target for the test of mounting procedure of the fibers and for the check of alignment of the fibers. A beam test at Tohoku Univ. ELPH is planned in the summer, 2019. After the beam test, we will complete the production of the fiber target with nine layers by the end of 2019. In 2019, we will purchase 15 EASIROC modules in addition to the existing 20 modules.

We plan to install the S-2S system in the K1.8 beam line in early 2020. We hope to have a better intensity of the K^- beam achieved in a pilot run of the J-PARC E05 in 2015. At that time, the K^- intensity was 6×10^5/ 5.52 seconds with the primary proton beam power of 39 kW. We observed about 50 events of signals for 10 days of data taking.

6. Run Plan of E70

Purpose of the E70 Run

After the preliminary results from the E05 run, these are the main purpose of the E70 new measurement with S-2S in 2-MeV missing-mass resolution;

(1) Separation of peaks, if existed, with a good energy resolution of 2 MeV (FWHM),

(2) Measurement of the width of the peak(s).

The energy resolution of 2 MeV enables us to separate the ^{11}B core excited states of which excitation energies are about 2-3 MeV depending on the strength of spin-spin interaction. In Fig. 45, Motoba's calculations taking account of the core excitations are shown for different interaction models. So, our measurement will be robust for any fine structures in this mass-number region. The largest binding

E70 Schedule

	2019.1	2019.4	2019.7	2019.10	2020.1	2020.3	2020.7	2020.10
Beam Line Detectors								
BFT	Ready at K1.8							
BDC3,4								
BH1								
BAC								
BH2								
S-2S								
QQD magnets	Ready at Tsukuba						Move from Tsukuba to J-PARC	Excitation test at K1.8
S-2S Detectors								
SDC1-2	Ready at J-PARC	Chamber Frame Construction	Operation test					
SDC3-5	DCs are ready at J-PARC	ASD Cards Production	Chamber Frame Construction	Operation test				
TOF	Magnetic field shields			Construction complete				
AC	Ready at J-PARC							
WC		Construction of Frame stand		Construction complete				
Active Target								
	Production of (xx'yy')x3 layers	Beam test at ELPH	Software development					
			Production of All (9) layers; Additional EASIROC modules		Beam test at K1.8			

1

Fig. 44. Construction and Installation Schedule of E70.

energy state gives us the lower limit of the ground state energy with a precision of 0.2 MeV, which is related to the real part of the potential Re(U_Ξ). The width of the peak might be less than a few MeV according to the recent lattice QCD calculation. On the other hand, if we observe one broad peak, the peak width would be larger than 10 MeV, so that the width could be measured easily, and we could obtain the information of imaginary part of the potential, Im(U_Ξ), with a precision better than 1 MeV.

Based on the results of the E05 run, we can surely estimate the yield of the ${}^{12}_{\Xi}$Be bound states in the case of S-2S, which has 55-msr solid-angle acceptance corresponding to a half of the SKS acceptance of 110 msr. The run conditions are summarized in Table IX.

MR beam power

The beam power from the main ring (MR) to the Hadron Experimental Hall is limited by the production target (T1) for secondary beams. At the time of the E05 pilot run, it was 39 kW, and produced 600 k K^- per spill at 1.8 GeV/c. The present T1 target can be used up to 52 kW. However not more than that. At this moment construction of a new T1 target made of Au which could sustain up to 85 kW is under way. It will be installed during the summer shutdown in 2019. There could be some inefficiency due to slits in the target to produce secondary beams. Here we assume at 85 kW delivered from the MR, it corresponds to 80 kW for secondary beam productions in the present T1 target. It will increase the K^- intensity by a factor of 2. In addition, we would like to shorten the operation cycle of the MR from the present 5.52 sec. to 4.7 sec. or less. It corresponds to a 100-kW operation of the MR. Even in this case the instantaneous beam rate is 0.6 M×(80/39)/1.7 sec.= 0.72 M/sec. which is well below the beam rate assumed in the original proposal, 1.4 M/0.8 sec. = 1.75

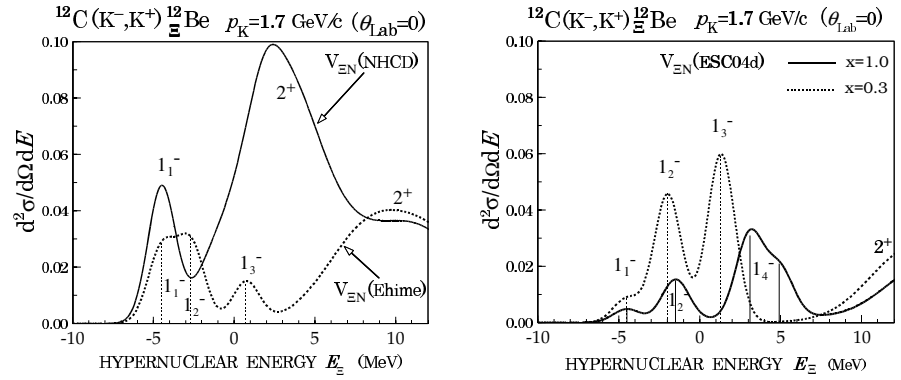

Fig. 45. Theoretical calculations of the excitation spectra for different interaction models. Prominent peak structures are seen with three 1^- states with about 3-MeV separations.

Run Conditions	E05 Run	E70 Run
K^- intensity (M/spill)	0.6	1.2
MR beam power (kW)	39	80
Spill cycle (s)	5.52	4.7
Target thickness (g/cm^2)	9.3	9
Spectrometer acceptance (msr)	110	55
kaon decay factor	1	0.7
DAQ efficiency	0.7	0.95
Missing-mass resolution (FWHM)	6 MeV	<2 MeV
Signal events/days of run	50/10 days	~110/20 days

Table IX. Run conditions in the E05 run and the expected condition for the E70 physics run with S-2S for ^{12}C(K^-, K^+)$^{12}_{\Xi}$Be reaction at 1.8 GeV/c.

M/sec.

Beam time request

After two weeks of beam tune and detector commissioning run, we would like to have the spectrometer tuning run with the scintillation fiber active target to obtain the $p(K^-, K^+)\Xi^-$ reaction data for about five days (30,000 Ξ^- events). We also need calibration runs for the active target by using the K^- beam for a few days. We will irradiate the beam through the whole volume of the scintillation fiber target. In a separated beam period, we would like to take physics data on ^{12}C(K^-, K^+) reaction at 1.8 GeV/c. After a 20-days of running time, we expect to have the number of 120 events in the bound region. It should be noted that the peak counts would be further enhanced owing to the better energy resolution of S-2S by a factor of three (6/2), at least. The flat background events in the pilot run, which is mainly due to π^+'s from K^- beam decay-in-flight around the target would be suppressed in the S-2S because of the good focusing property of the spectrometer.

7. Summary

In the J-PARC E70 experiment, we aim for establishing the existence of $\Xi-$hypernuclei as clear peak structures. A new spectrometer S-2S is constructed for the high energy resolution spectroscopy

with (K^-, K^+) missing-mass measurement. By combining with an active scintillation fiber target, the energy resolution of better than 2 MeV (FWHM) will be achieved with a thick target of 10 g/cm^2. The real part and imaginary part of the ΞN potential will be measured in high accuracy.

Here, we would like to propose the following beam time listed in Table X.

Run	beam time
Detector and Beam Commissioning	$\gtrsim$2 weeks
$p(K^-, K^+)\Xi^-$	5 days
Active target calibration	3 days
$^{12}\mathrm{C}(K^-, K^+)^{12}_{\Xi}\mathrm{Be}$	20 days

Table X. Beam time request for E70 with S-2S spectrometer.

Detector commissioning and beam tuning runs should be allocated separately from the following runs. Then, after these commissioning, we would like to have calibration data taking for the $p(K^-, K^+)\Xi^-$ reaction and for the active target for 8 day. For both calibration runs we are going to use the fiber scintillation target. At this stage, we might have a short break to analyze the data taken. After confirming the system is working well, we will have the physics data taking by using the fiber scintillation target (10 g/cm^2).

In order to perform these data taking, it is crucial that the primary beam power reaches about 100 kW effectively with a new production target and a shorter spill cycle.

References

[1] H. Tamura *et al.* [J-PARC E13 Collaboration], JPS Conf. Proc. **17**, 011004 (2017).
[2] H. Takahashi *et al.*, Phys. Rev. Lett. **87**, 212502 (2001).
[3] J. K. Ahn *et al.* [E373 (KEK-PS) Collaboration], Phys. Rev. C **88**, no. 1, 014003 (2013).
[4] T. Harada and Y. Hirabayashi, Nucl. Phys. A **759**, 143 (2005).
[5] K. Sasaki *et al.* [HAL QCD Collaboration], PTEP **2015**, no. 11, 113B01 (2015).
[6] A. Gal, E. V. Hungerford and D. J. Millener, Rev. Mod. Phys. **88**, no. 3, 035004 (2016).
[7] P. Demorest, T. Pennucci, S. Ransom, M. Roberts and J. Hessels, Nature **467**, 1081 (2010).
[8] J. Antoniadis *et al.*, Science **340**, 6131 (2013).
[9] T. Fukuda *et al.*, Phys. Rev. C **58** (1998) 1306.
[10] P. Khaustov *et al.*, Phys. Rev. C **61** (2000) 054603.
[11] M. Kohno and S. Hashimoto, Prog. Theor. Phys. **123** (2010) 157.
[12] M. Kohno, Phys. Rev. C **81** (2010) 014603.
[13] K. Nakazawa *et al.*, Prog. Theor. Exp. Phys. **2015** (2015) 033D002.
[14] T. Gogami *et al.*, Phys. Rev. C **93**, no. 3, 034314 (2016).
[15] T. Harada, Y. Hirabayashi and A. Umeya, Nucl. Phys. A **914**, 85 (2013).
[16] C. B. Dover and A. Gal, Ξ *Hypernuclei*, Annals Phys. **146**, 309 (1983).
[17] T. Gogami, N. Amano, S. Kanatsuki, T. Nagae and K. Takenaka, Nucl. Instrum. Meth. A **817**, 70 (2016).
[18] L. Tang *et al.* [HKS Collaboration], Phys. Rev. C **90**, no. 3, 034320 (2014).
[19] T. Motoba *et al.*, Nucl. Phys. A **827** (2009) 318c-320c.